

GECO: Geometrically Consistent Embedding with Lightspeed Inference

Regine Hartwig

Dominik Muhle

Riccardo Marin

Daniel Cremers

TU Munich

Munich Center for Machine Learning

{regine.hartwig, dominik.muhle, riccardo.marin, cremers}@tum.de

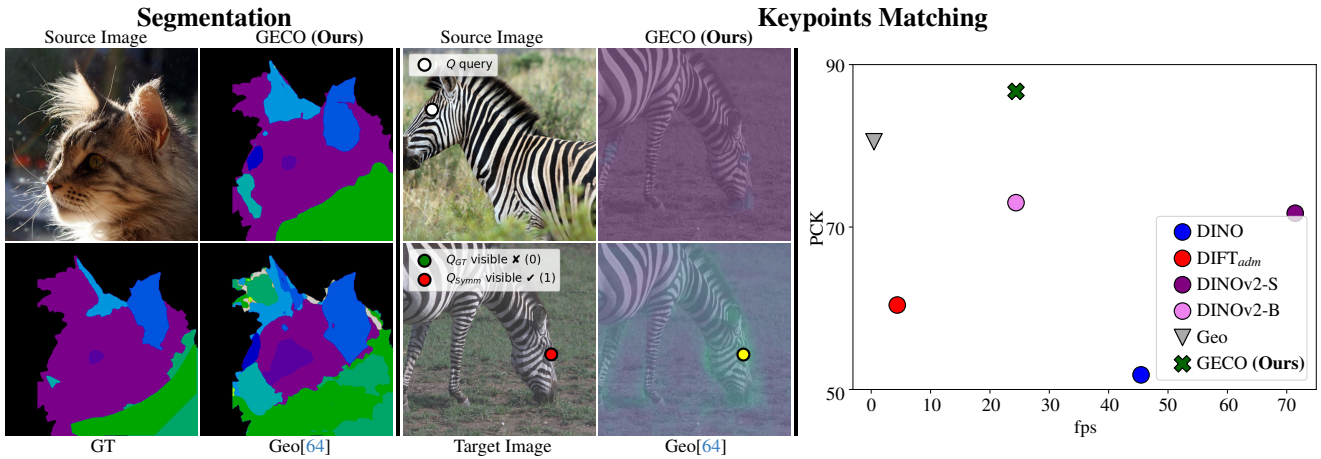


Figure 1. We propose **GECO**, an optimal-transport-based approach for learning geometrically consistent visual features. Characterizing geometric properties, like distinguishing left/right eyes or front/back legs, remains challenging even for sophisticated methods. For instance, in the keypoint transfer example, showing a zebra, Geo [64] confuses the eyes, while our features have low similarity. Our method learns robust feature representations, achieving high accuracy while remaining lightweight and efficient at inference time (plot on the right), enabling real-time applications at 30fps. Our feature embedding exhibits a continuous and structured understanding of objects, making it highly effective for image segmentation (left) and precise keypoint matching, even in challenging scenarios involving occlusions (middle, with attention maps overlaid on the target images).

Abstract

Recent advances in feature learning have shown that self-supervised vision foundation models can capture semantic correspondences but often lack awareness of underlying 3D geometry. GECO addresses this gap by producing geometrically coherent features that semantically distinguish parts based on geometry (e.g., left/right eyes, front/back legs). We propose a training framework based on optimal transport, enabling supervision beyond keypoints, even under occlusions and disocclusions. With a lightweight architecture, GECO runs at 30 fps, 98.2% faster than prior methods, while achieving state-of-the-art performance on PFPascal, APK, and CUB, improving PCK by 6.0%, 6.2%, and 4.1%, respectively. Finally, we show that PCK alone is insufficient to capture geometric quality and introduce new metrics and insights for more geometry-aware feature learning. <https://reginehartwig.github.io/publications/geco/>

1. Introduction

Vision Foundation models either trained only on images [14, 42] or text-image pairs [47] produce flexible features that can be applied across various tasks such as image generation, style transfer, and correspondence estimation. While these models perform well across a range of applications, they are constrained by their limited ability to distinguish between geometric properties [16]. For instance, they may struggle to differentiate between left and right eyes or the legs of a chair, issues that have been explored in the context of the Janus problem [16, 64]. Since they are trained using consistency between self-augmented images, including flipping, they often do not differentiate between symmetric parts, and are even encouraged to learn features that are invariant to such transformations. These models often encounter challenges like ambiguous features for semantically similar regions and confusion due to occlusions. Such mismatches can lead to severe artifacts in practical downstream applications, such as a category template reconstruction pipeline incorrectly reconstructing 5-legged

animals or chairs [39]. More advanced approaches, such as Geo [64], enhance SD+DINO features [65] to address left-right ambiguities. However, despite its advancements, this method is often too slow, taking several seconds for a single prediction, making it impractical and difficult to scale.

Our work proposes **GEometrically COnsistent** embeddings, an efficient and robust approach to address this problem without compromising efficiency. A key limitation of previous methods is their reliance on argmax-based assignments during training, which inherently assumes the key-point to be visible in both views and fails to account for (dis-)occlusions. Our intuition is that it therefore does not provide a strong supervision signal for the model to learn meaningful features. Specifically, it overlooks the fact that we are dealing with a partial assignment problem. For instance, in cases of occlusion, annotated information is ignored during training, even though it could help the model learn the correct bin assignment. Furthermore, the supervision signal is sparse: only a few annotated points are used, while the rest of the image contributes nothing to the training process. Although soft-argmax assignments with Gaussian perturbations of the position have been proposed to mitigate this issue, they tend to introduce blurring and ultimately still depend on an argmax operation, which is not a natural fit for the underlying assignment problem. Instead, to account for the partial assignments and differentiability, we introduce a novel *soft assignment loss* that leverages optimal transport on top of vision foundation models, leading to a nuanced and discriminative feature learning process. This loss function provides strong supervision feedback, allowing our module to learn distinctive features that effectively differentiate symmetric keypoints. The optimal transport loss is based on the Sinkhorn algorithm [11], which enables a differentiable soft assignment formulation for back-propagation.

Importantly, unlike previous approaches [48, 50], our method does not rely on cross-attention between image pairs, the marginal distributions of the optimal transport module are created and enforced differently (see supplementary), and the module operates without trainable parameters. As a result, our model is a *feature encoder rather than a feature matcher*. GECO focuses on robust representation learning rather than direct correspondence estimation between two images.

Concretely, we employ a pre-trained model and refine it through LoRA adaptation [26]. Leveraging DINOv2 ensures computational efficiency, enabling more extensive data augmentation compared to prior methods and further enhancing the robustness of learned features.

Our method outperforms the state of the art while being **faster and smaller by two orders of magnitude w.r.t. the closest competitor** (40 ms vs 2127ms; 332MB vs 9GB). We perform an extensive evaluation, demonstrating our su-

periority on the classical PCK@0.1 metric on CUB, APK, and PFPascal datasets [22, 55, 64]. We also extend our analysis to complement the information provided by the PCK metric, which we found might not be indicative of some prediction modes. Thanks to this, we demonstrate that our better performance directly derives from a better geometrical understanding, which also leads to a more focused and calibrated prediction, distributing similarity on the correct area and assigning occluded parts to the bin (see Fig. 1).

In summary, our contributions are:

1. We propose a novel loss function and a lightweight architecture for image representation learning, leveraging optimal transport-based soft assignment;
2. Our formulation leads to geometrically-aware features, enabling state-of-the-art performance on correspondence estimation while being significantly more efficient. It surpasses geometrically-aware competitors on multiple datasets while *reducing computation time by 98%*, maintaining the speed of the lightweight backbone.
3. We conduct an extensive analysis of the common PCK metric and complement it with object part segmentation evaluation on PascalParts. Our method effectively separates parts, indicating that it learns meaningful, dense feature representations.

Our implementation will be instrumental for researchers interested in downstream tasks of geometry-aware encoders.

2. Related Work

Deep features Self-supervised and unsupervised methods have gained popularity [3–5, 17, 20, 23, 24, 42], but if trained on image-level objectives [3–5, 20, 24] often fail to capture fine spatial details [1, 54]. Patch-based methods like DINOv2 [42], inspired by [66], learn effective feature representations for tasks like clustering and matching. Diffusion models [14, 47] have become powerful generative models, with (Clean-)DIFT [49, 51] enabling dense feature extraction for vision tasks. While DINOv1, DINOv2 [4, 42], and DIFT [51] work well for zero-shot tasks [1, 19, 21, 25, 54], including semantic correspondence finding, they often struggle with geometric awareness, especially left-right distinctions [7, 16], potentially due to image-flipping augmentations [42]. Stable Diffusion (SD) features [14] encode more geometry than DINOv1 [4], but still lack left-right distinction, exposing limitations in spatial understanding, which can cause problems in 3D reconstruction [31, 35, 39].

Geometry-aware matching Several methods address key-point matching for rigid objects, such as SuperPoint [13] and SuperGlue [48], which use homography supervision. LOFTR [50] improves upon this with dense optimal transport matching. These approaches rely on (cross-)attention

and learnable optimal transport layers for sparse labels. Recent methods like DUST3R, MAST3R, Fast3R [33, 57, 62] assume rigid motion, limiting their applicability to more complex cases. Our method, GECO, focuses on learning features rather than matching and handles deformable objects and complex geometries. Deformable objects complicate training, as constraints (*e.g.* epipolar) are not available. Improving matching of deformable objects, CATs++ [9] uses attention layers, LCorrSan [27] estimates dense flow via correlation layers, [8] uses functional maps, and [34, 53] optimize dense probabilities. These methods focus on correspondence estimation. Our approach prioritizes feature learning, not matching.

Geometry-aware representation Recent work [56, 58, 60, 63] uses rigid inter-instance supervision for learning features with geometric awareness. Others focus on geometry-aware deformable intra-instance representation learning: Using 3D supervision, concurrent work [18, 32, 45] achieve good results on the geometric-aware matching task and a similar speedup as our method. Unlike our focus on speed and efficiency, [61] targets matching performance using additional correspondence supervision and Diffusion Features. However, the need for extra signals and lack of real-time capability limit its practical applicability. Earlier works like AnchorNet [40] use category-level supervision for geometry-aware features. DHF [36] fine-tunes diffusion features for semantic matching with a sparse contrastive loss on keypoints. Unsup [52] and Sphere [37] map to spherical coordinates with category and viewpoint supervision, while [15] also uses the spherical geometric prior without supervision. Completely unsupervised, SCOPS [28] enforces equivariance for co-part segmentation, while [10] uses contrastive learning for part discovery. We consider Geo [64] the most closely related work to ours. It uses a sparse contrastive loss with keypoint annotations and a soft argmax operator for feature enhancement. However, its reliance on SD features results in slower inference, category annotation dependency, and larger model size. Additionally, the extra parameters introduced by their head are significant, increasing the potential for overfitting.

Training with sparse correspondences To leverage sparse correspondence during training, a common approach applies an argmax operator [36, 64] with a sparse contrastive loss [29, 46]. While effective in some domains, this method, when used with keypoint annotations [36], provides a learning signal to only a small subset of annotated patches visible in both images, resulting in suboptimal feature representations [64]. We leverage optimal transport (OT) [11, 12] not as a matching module, but to define a structured soft assignment loss. Specifically, we employ the Sinkhorn algorithm [11, 12, 43], a differentiable

OT solver that produces dense supervision across all image patches [2, 30, 59] by minimizing the cost to transport mass between distributions. Unlike prior work [48, 50], our formulation requires no additional trainable parameters, resulting in more broadly applicable and task-agnostic features.

Our positioning Our method builds on a lightweight and efficient DINOv2-B backbone, fine-tuned using LoRA [26] to improve both computational efficiency and memory usage. To address the core challenges of sparse annotations and (dis-)occlusions in loss design, we introduce a soft optimal transport layer. This layer delivers a learning signal to all patches, effectively utilizing the full set of available annotations and enabling the learning of robust and discriminative feature representations.

3. Background

Argmax matching Considering a source image S and target one T , both equipped with a set of patches represented by their indices $\mathcal{I} := \{i_1, \dots, i_l\}$ and $\mathcal{J} := \{j_1, \dots, j_m\}$ and their d -dimensional features $\mathbf{X}^s \in \mathbb{R}^{l \times d}$ and $\mathbf{X}^t \in \mathbb{R}^{m \times d}$ respectively. Given a query location i , the corresponding \hat{j} on the target can be received by:

$$\hat{j} = \arg \max_j \langle \mathbf{X}_i^s, \mathbf{X}_j^t \rangle. \quad (1)$$

While simple, argmax matching suffers from several drawbacks. It introduces ambiguity, as multiple geometrically distinct source locations can map to the same target point (*e.g.*, left and right eyes both matching to one eye). It does not account for occlusions, often resulting in incorrect assignments with low similarity. Moreover, it imposes hard, one-hot assignments that assume equal mass per patch across images, limiting its ability to handle scale differences or partial matches. Crucially, it ignores the global structure of the assignment, focusing only on local maxima, which leads to sparse gradients and hinders effective training. We instead formulate matching as an optimal transport problem. To handle occlusions, we introduce a dustbin entry in the assignment matrix, and employ a soft, iterative solver [11, 12] that provides meaningful gradients for all features, improving training stability and convergence.

Optimal Transport formulation Suppose we have pairs of patches $(i, j) \in \mathcal{I} \times \mathcal{J}$. We solve for an assignment between two images [42, 48] by using the cosine similarity of the features as score matrix \mathbf{C} with

$$\mathbf{C}_{i,j} = \langle \mathbf{X}_i^s, \mathbf{X}_j^t \rangle \in [-1, 1]. \quad (2)$$

In order to model occlusions properly, we augment the vectors with a dustbin at $l' = l + 1$ and $m' = m + 1$, which gets assigned a threshold parameter $z \in \mathbb{R}$:

$$\mathbf{C}_{i_{l'}, i_{m'}} = \mathbf{C}_{i_{l'}, j} = \mathbf{C}_{i, i_{m'}} = z \quad \forall i, j \in \mathcal{I} \times \mathcal{J}. \quad (3)$$

We then solve for an assignment matrix $\mathbf{P} \in U(\mathbf{a}, \mathbf{b})$, where

$$U(\mathbf{a}, \mathbf{b}) := \left\{ \mathbf{P} \in \mathbb{R}_+^{i_{l'} \times i_{m'}} \mid \mathbf{P} \mathbf{1}_{i_{m'}} = \mathbf{a}, \mathbf{P}^T \mathbf{1}_{i_{l'}} = \mathbf{b} \right\}, \quad (4)$$

$\mathbf{a} \in \Sigma_{i_{l'}}$, and $\mathbf{b} \in \Sigma_{i_{m'}}$, i.e. the marginalizations of P (see supplementary) are in the respective simplex $\Sigma_n := \{ \mathbf{x} \in \mathbb{R}_+^n : \mathbf{x}^T \mathbf{1}_n = 1 \}$. The assignment can be obtained by solving the OT problem

$$\hat{\mathbf{P}} = \arg \max_{\mathbf{P} \in U(\mathbf{a}, \mathbf{b})} \langle \mathbf{P}, \mathbf{C} \rangle. \quad (5)$$

To provide gradients for all input features during training, we use a regularized OT, which yields a smooth and differentiable assignment

$$\hat{\mathbf{P}}^\lambda = \arg \max_{\mathbf{P} \in U(\mathbf{a}, \mathbf{b})} \langle \mathbf{P}, \mathbf{C} \rangle + \lambda H(\mathbf{P}), \quad (6)$$

with $H(\mathbf{P}) = -\sum_{i,j} \mathbf{P}_{ij} \log \mathbf{P}_{ij}$ being the entropy of the assignment matrix. For $\lambda > 0$ the entropy regularization promotes smoother, less sparse assignments, resulting in a differentiable soft assignment $\hat{\mathbf{P}}^\lambda$ that provides a gradient signal for all input features. Furthermore, changing the problem to an unbalanced OT problem, using additionally the KL-divergence as a regularizer [44], helps in the case of unbalanced marginals \mathbf{a} and \mathbf{b} , meaning, that the amount of mass that needs to be assigned is not equal for both marginals

$$\begin{aligned} \hat{\mathbf{P}}^{\lambda, \alpha, \beta} = \arg \max_{\mathbf{P} \in \mathbb{R}_+^{i_{l'} \times i_{m'}}} & \langle \mathbf{P}, \mathbf{C} \rangle + \lambda H(\mathbf{P}) \\ & - \alpha \text{KL}(\mathbf{P} \mathbf{1}_{i_{m'}} \parallel \mathbf{a}) - \beta \text{KL}(\mathbf{P}^T \mathbf{1}_{i_{l'}} \parallel \mathbf{b}). \end{aligned} \quad (7)$$

In general, for formulating the OT problem, we need to know the distributions of \mathbf{a} and \mathbf{b} . However, using the unbalanced OT problem, we can relax the requirement of knowing the marginals, which is crucial for our application, as we do not have access to the ground truth marginals, but only estimates.

4. Method

We now describe our approach, including the feature learning module and the differentiable OT layer without learnable parameters, which processes the cosine similarity of patches. Finally, we introduce a loss function that encourages higher output probabilities for positive and bin pairs and lower probabilities for negative pairs.

Architecture Our architecture is simple, efficient, and interpretable (see Fig. 2). We use a pre-trained DINOv2-B model [42], kept frozen during training, and adapt it with a LoRA adapter [26] of rank 10.

Differentiable OT layer We compute the cosine similarity of all features from S and T , including the background, obtaining a cosine similarity matrix. We augment this matrix with an additional row and column, setting a bin threshold of $z = 0.3$, and obtaining the score Matrix \mathbf{C} .

Next, we pass \mathbf{C} to a differentiable optimal transport (OT) layer, which computes the optimal transport plan between the features of S and T . Unlike previous works [48, 50], which enforce hard constraints on the boundaries \mathbf{a} and \mathbf{b} , we adopt a KL-regularized soft assignment (Eq. (7)), allowing greater flexibility. Additionally, the OT layer has no learnable parameters and contributes to the loss function rather than being part of the model itself.

The marginals \mathbf{a} and \mathbf{b} of the multivariate probability matrix $\hat{\mathbf{P}}$ are estimated using mask annotation and a method to determine the amount of the visible mass of the shape. Details on this are provided in the supplementary material. The Sinkhorn-Knopp algorithm runs for 10 iterations, producing a probability matrix $\hat{\mathbf{P}}^{\lambda, \alpha, \beta}$ with the same dimensions as the score matrix \mathbf{C} . The hyperparameters of the OT layer are $\lambda = 0.1$, $\alpha = 10$, and $\beta = 10$.

Binary cross entropy loss As we do not have access to the ground truth matrix \mathbf{P} , which assigns all features of S to all features of T , but only to the sets of positive, negative, and bin correspondences $\mathcal{M}^+, \mathcal{M}^-, \mathcal{M}^0 \subset \mathcal{I} \times \mathcal{J}$, we formulate our loss only on these sets. Using a binary cross-entropy loss, we train the model to predict the correct values at some sparse entries of the assignment matrix \mathbf{P} by

$$\mathcal{L} = - \sum_{(i,j) \in \mathcal{M}^+ \cup \mathcal{M}^0} \log \hat{\mathbf{P}}_{i,j}^{\lambda, \alpha, \beta} - \sum_{(i,j) \in \mathcal{M}^-} \log(1 - \hat{\mathbf{P}}_{i,j}^{\lambda, \alpha, \beta}). \quad (8)$$

We additionally add matches between foreground and background features to the set \mathcal{M}^- , which are not part of the ground truth, to enforce the model to learn to distinguish between the two.

5. Experiments

In this section we extensively evaluate our method compared to baselines, analyzing their capability of understanding geometry. First, in Sec. 5.1, we utilize the established PCK metric on different datasets, where we show that we are on par and better than the previous state-of-the-art. We also provide a detailed analysis of the limitations of PCK, and propose new metrics to inspect geometric knowledge of the features. In Sec. 5.2, we show that our method, using centroid clustering, also performs well on the pixel-level classification task without additional training, relying on a simple supervised classifier. This indicates that our approach effectively learns meaningful features.

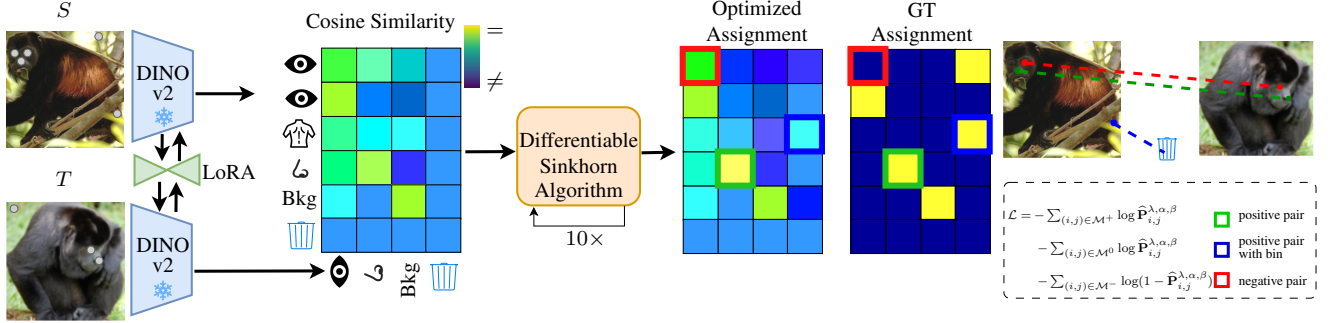


Figure 2. **Architecture and Training.** At training time, our method takes a pair of images composed of a source S and targets one T , and obtains features through a DINOv2 [42] frozen model complemented with a LoRA adapter [26]. The features are used to compute the matching by cosine similarity associations between all patches. For visualization purposes, we show the matrix for the landmarks (grey dots). We pass the obtained matrix to a differentiable Optimal Transport Layer that, in a few iterations, obtains the predicted assignment. We compare this with the ground truth, and we use this as a supervision signal for our method. Our training objective also provides supervision signals on negative keypoint pairs and, thanks to the “bin” category, on keypoints that do not even have a visible counterpart in one of the two images.

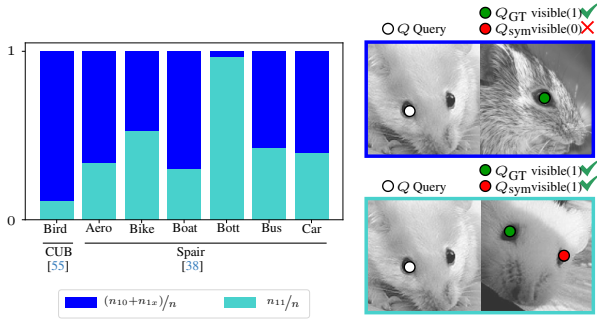


Figure 3. **PGCK Dataset imbalance.** We report keypoint pairs grouping under our PGCK subdivision. n_{11} counts only the pairs for which a geometric mismatch is possible. Other keypoint pairs (having no geom. counterpart/ with occluded geom. counterpart) are counted in $(n_{10} + n_{1x})$. Due to the high category imbalance, geometric error modes impact the overall PCK differently.

5.1. Analysis with (and of) PCK

Percentage of correct keypoints (PCK) The percentage of correct keypoints (PCK) is a widely used metric for evaluating the performance of correspondence estimation methods. We take an image pair, where keypoint matches are annotated, and evaluate how many query points Q are correctly reprojected into the second view (see Figs. 5 and 6). A reprojection is labeled as correct if the distance ϵ between predicted and annotated location Q_{GT} is less than a threshold α_{img} of the image size or α_{bbox} of the bounding box size. Following the evaluation protocol of previous work [51], we use argmax matching for building assignments and reprojection only in one direction. In this work, we consider the PCK_{point} @ α_{img} version of it, where the percentage of correct keypoint reprojections per point is

\hat{n}/n , the fraction of the sum of correctly reprojected points \hat{n} across all image pairs to all annotated point pairs n . It is interesting to note that PCK considers only keypoint pairs in which the query keypoint is visible in the target image. Hence, it does not evaluate a model’s performance when the reprojection is not visible in the target image, but its symmetric counterpart is (see Fig. 5, first four rows). To address this, we also report performance using qualitative results.

Percentage of geometry-aware correct keypoints (PGCK) Although PCK has played an important role in evaluating matching methods, we believe it is insufficient to depict the methods’ understanding of geometry. We propose to break down the proportion between the correct reprojections \hat{n} and the total number of keypoints n into different sets. Specifically, we separate the evaluation of query points that have a visible symmetric counterpart in the target image (n_{11} , an example in Fig. 3, second row) from those that have a symmetric counterpart but are occluded in the target, and those for which a symmetric counterpart does not exist (n_{10} and n_{1x} respectively; example of the first in Fig. 3, first row). PCK can then be divided in:

$$PCK_{point} = \frac{\hat{n}}{n} \quad (9)$$

$$= \frac{\hat{n}_{10} + \hat{n}_{11} + \hat{n}_{1x}}{n_{10} + n_{11} + n_{1x}} \quad (10)$$

$$= \underbrace{\frac{\hat{n}_{10}}{n_{10}}}_{\substack{Q_{GT} \checkmark \\ Q_{Symm} \times}} + \underbrace{\frac{\hat{n}_{11}}{n_{11}}}_{\substack{Q_{GT} \checkmark \\ Q_{Symm} \checkmark}} + \underbrace{\frac{\hat{n}_{1x}}{n_{1x}}}_{\substack{Q_{GT} \checkmark \\ Q_{Symm}^-}}, \quad (11)$$

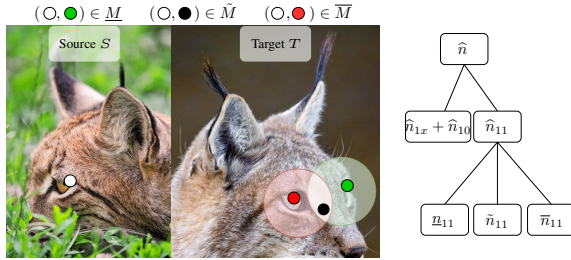


Figure 4. **Geometric Ambiguity of PGCK.** In the case of symmetric correspondences, the PCK metric does not account for ambiguous assignments of true positive correspondences. The **Green dot** around the annotated match will collect an assignment that results in a true positive match, the **Red dot** collects symmetric mismatches. In cases where the symmetric counterpart keypoint is sufficiently close, the circles overlap. These points can not be unambiguously assigned to either keypoint. The PCK metric still counts them as true positives. Points falling into the ambiguous set area are collected in \tilde{M} and make up around 50% of the prediction for all investigated methods.

where the number of keypoint pairs $n = n_{10} + n_{11} + n_{1x}$ and number of correct reprojections $\hat{n} = \hat{n}_{10} + \hat{n}_{11} + \hat{n}_{1x}$. Although PCK comprehends all these quantities, we see that evaluation on n_{10} and n_{1x} is less informative than those on set n_{11} , where actually the method could get confused by the presence of a symmetric element. For evaluating the geometric reasoning, we are interested only in the number \hat{n}_{11} , where the model correctly matches the query keypoint when the symmetric counterpart is also visible in the target image. We can see its relevance by measuring the distribution of the annotated point pairs for the CUB and SPair datasets in the three categories. We report the counting in Fig. 3. In the CUB dataset, $n_{1x}/n = 78\%$ of the keypoint pairs have no symmetric counterpart. For the remaining 22% of the keypoint pairs, in only 11% of the keypoint pairs, the symmetric counterpart is also visible in the second view. The SPair dataset has a high variation between the categories, with the highest value for the bottle category (97%) and the lowest for the bird category (23%). In the following, we report both evaluations using PCK metric and our proposed split. We call such division *Percentage of geometry-aware correct keypoints* (PGCK).

Geometric Ambiguity Although \hat{n}_{11}/n_{11} show informativeness about geometric knowledge of models, to complete our analysis, we also highlight a special set that is worth further investigation. Specifically, the set \tilde{M} with $|\tilde{M}| = \tilde{n}_{11}$ contains point pairs where the predicted location is close (with a distance smaller than the defined radius) to Q_{GT} and Q_{Symm} as shown in Fig. 4.

Therefore, success in these cases does not directly measure geometric knowledge, as it “cheats” the metric by pre-

| | Unambiguous Correct Pred. $\frac{\hat{n}_{11}}{n_{11}} \uparrow$ | ambiguous $\frac{\hat{n}_{11}}{n_{11}}$ | Unambiguous Wrong Pred. $\frac{\bar{n}_{11}}{n_{11}} \downarrow$ |
|-------------------------|--|--|--|
| DINO [4] | 17.0 | 38.8 | 16.0 |
| DIFT _{ad} [51] | 25.2 | 43.8 | 8.4 |
| DINOv2-S [42] | 25.1 | 50.9 | 13.8 |
| DINOv2-B [42] | 24.5 | 51.8 | 16.0 |
| Geo [64] | 36.2 | 53.1 | 2.9 |
| GECO (Ours) | 40.0 | 53.2 | 2.3 |

Table 1. **Geometric ambiguity** Analysis of PGCK on APK [64]. We outperform previous work in the unambiguous geom. correct matching (left) by 3.8 %, while our method disregards more of the unambiguously wrong pairs (right). The best scores are highlighted in **bold**.

dicting points in the middle of the two. To compensate for this, it is possible to derive two further measures. First, the **unambiguous true positives U-TP** n_{11}/n_{11} , which measures the cardinality $|\underline{M}| = \underline{n}_{11}$ of the subset, which contains correctly matched keypoint pairs, where Q_{Symm} is far enough away from the predicted position. Second, the **false correspondences** \bar{n}_{11}/n_{11} , which measures the cardinality $|\bar{M}| = \bar{n}_{11}$ of the subset, which contains wrongly matched keypoint pairs, where Q_{GT} is far enough away from Q_{Symm} to be considered as a completely wrong match. As we will see later, the high number of keypoint pairs \tilde{n}_{11} indicates that the commonly used radius $\alpha_{img} = 0.1$ is too big for the PCK metric. A further analysis of how the subsets behave for other values of α_{img} is provided in the supplementary material.

5.1.1. Evaluation

Data In this experiment, we evaluate our method on datasets with pairwise keypoint annotations. Specifically, we use the CUB dataset [55], selecting 10,000 image pairs of at random, as well as SPair [38], PFPascal [22], and APK [64], which provide predefined image pairs. Since PFPascal lacks symmetric counterpart annotations, we assess only the standard PCK metric on this dataset.

Results The quantitative PCK analysis on PFPascal, APK, and Spair is shown in Tab. 2. Our method surpasses previous state-of-the-art by 6.0% on PFPascal, 6.2% on APK, and 4.1% on CUB, while being nearly two orders of magnitude faster. Notably, Geo, using DINOv2-B and Stable Diffusion features, generalizes less well on CUB than DINOv2-S. In fact, the only dataset where Geo outperforms our method is Spair, indicating that is not a general purpose model. Detailed PCK results for PFPascal, APK, and Spair appear in the supplementary material. We provide an in-depth APK evaluation in Tab. 1, where our method improves across all n_{11} splits and consistently outperforms Geo in three of four cases (see supplementary).

| PFPascal [22] | | APK [64] | | Spair [38] | | CUB [55] | |
|-------------------------|-------------|-----------|-----------|-------------|-----------|-------------|-------------|
| | PCK↑ | | time[ms]↓ | | PCK↑ | | time[ms]↓ |
| DINO [4] | 65.3 | | 26 | 51.8 | 22 | 48.4 | 25 |
| DIIT _{ad} [51] | 72.5 | | 221 | 60.4 | 228 | 59.3 | 222 |
| DINOv2-S [42] | 85.5 | 14 | | 71.7 | 14 | 66.3 | 15 |
| DINOv2-B [42] | 86.0 | | 45 | 73.0 | 40 | 67.1 | 38 |
| Geo [64] | 86.1 | | 2141 | 80.5 | 2127 | 90.1 | 2159 |
| Sphere [37] | 88.5 | | 2152 | 75.2 | 2144 | 74.5 | 2164 |
| GECO (Ours) | 92.1 | | 45 | 86.7 | 40 | 85.2 | 38 |
| | | | | | | | 92.5 |
| | | | | | | | 43 |

Table 2. Quantitative evaluation of PCK on PFPascal [22] (Left), APK [64] (Middle), Spair [38] (Middle), and CUB [55] (Right). We report the PCK@ $\alpha = 0.1$ for four different datasets on the test split. Our method outperforms competitors in three out of four datasets by 6.0% on PFPascal, 6.2% on APK, and 4.1% on CUB, while ~ 2 orders of magnitude faster. In contrast, does not generalize well to CUB, where it lags behind DINOv2-S. Both Geo and our method are trained on PFPascal [22], APK [64], and Spair [38], while Sphere is trained solely on Spair. The best scores are highlighted in **bold**. Methods are considered to be on par if their performance difference is less than 0.5%. We mark **CUB [55]** in blue to highlight that it has not been seen at training time.

5.2. Feature Space Segmentation

The PCK metric evaluates correspondence accuracy based on a limited set of keypoints. While effective at those points, it does not assess the dense feature space, which is crucial since methods are trained on these annotations. We propose evaluating the feature space by partitioning it into semantically meaningful parts using only Euclidean distance to part-specific representation vectors. This indicates whether the learned features capture meaningful, consistent structures within the image.

5.2.1. Evaluation

Centroid Clustering To analyze the feature-space structure, we compute centroids for each annotated object part, assessing whether the model can separate parts using only Euclidean distance to these centroids. We first gather sets of feature vectors corresponding to each annotated part and then compute their median as the part representations. On the test set, each patch is assigned to the nearest centroid based on Euclidean distance, evaluating the model’s ability to discriminate parts purely from the learned features.

Data We evaluate dense features using part annotations from PascalParts [6], which offer consistent, category-specific labels for assessment.

Results Our learned feature representations reliably distinguish semantically similar parts with distinct geometric properties. Figs. 7 and 8 show qualitative examples where our method accurately separates challenging regions such as left/right eyes, wings, and ears. In contrast, the foundation model often exhibits artifacts, marked by red arrows and circles in the figure. Geo [64], which uses Gaussian sampling around keypoints during training, tends to assign overly broad regions to the eyes. Quantitative and qualitative confusion matrix analyses in the supplementary highlight ge-

ometric ambiguities in foundation models. Our method achieves geometrical awareness comparable to Geo [64] and shows greater consistency on non-geometric parts.

5.3. Runtime

Procedure We measure inference time by running a forward pass (excluding image loading) on 1,000 images per dataset using an RTX A4000 GPU, averaging the results. All models are evaluated with a batch size of 1.

Results Our timing results can be found in Tab. 2. For DINOv2 our measurements are consistent with those reported in the NVIDIA NCG catalog [41], falling within the same order of magnitude. The addition of our “light-speed” adapter introduces minimal overhead, contributing less than 0.5 ms to DINOv2-B’s baseline runtime of approximately 40 ms. Importantly, the performance of the original DINOv2 on the geometric matching task is not as strong. On the other hand, Geo’s [64] geometrically aware features, which rely on diffusion models, result in much longer inference times exceeding 2 seconds. Furthermore, in contrast to Geo [64], our method benefits from lower memory requirements, enabling efficient batch processing at inference time, which would further amplify the speed performance gap, making our method significantly faster and more scalable for practical applications.

6. Conclusion

We present a fast and efficient representation learning method based on optimal transport loss, achieving state-of-the-art PCK performance and improved geometric understanding. Our structured analysis highlights underexplored aspects of feature learning using PCK subdivisions and centroid clustering. While our method is lightweight and generalizes well, it relies on sparse keypoint supervision and is currently limited to categories with available annotations.

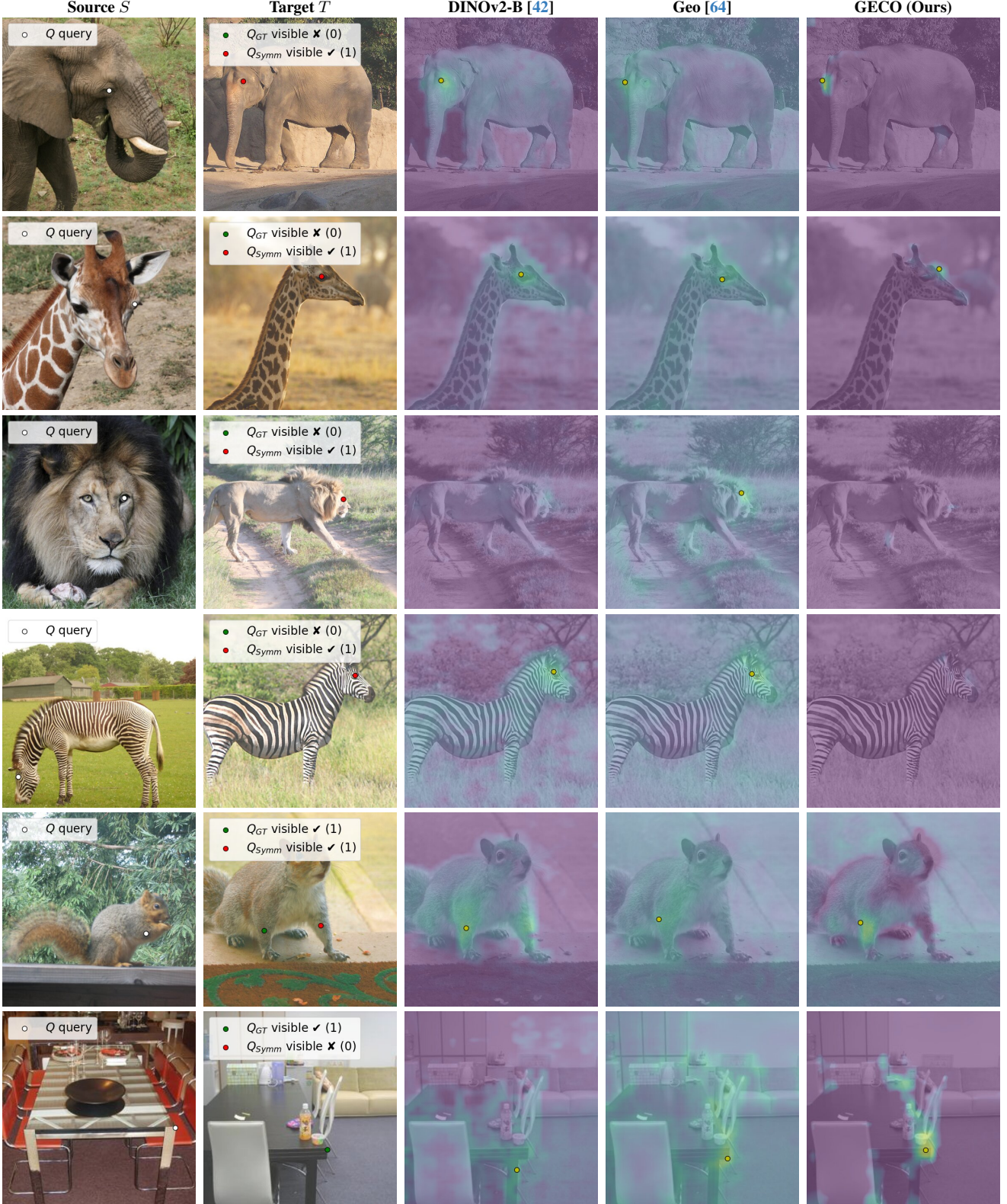


Figure 5. Qualitative results on correspondence estimation for APK [64], and PFPascal [22]. (Top two rows) The model accurately locates the ground truth correspondence, becoming visible with slight movement, while ignoring symmetric counterparts. (Third, Fourth row) When the symmetric counterpart is occluded, attention is uniformly low across the image.

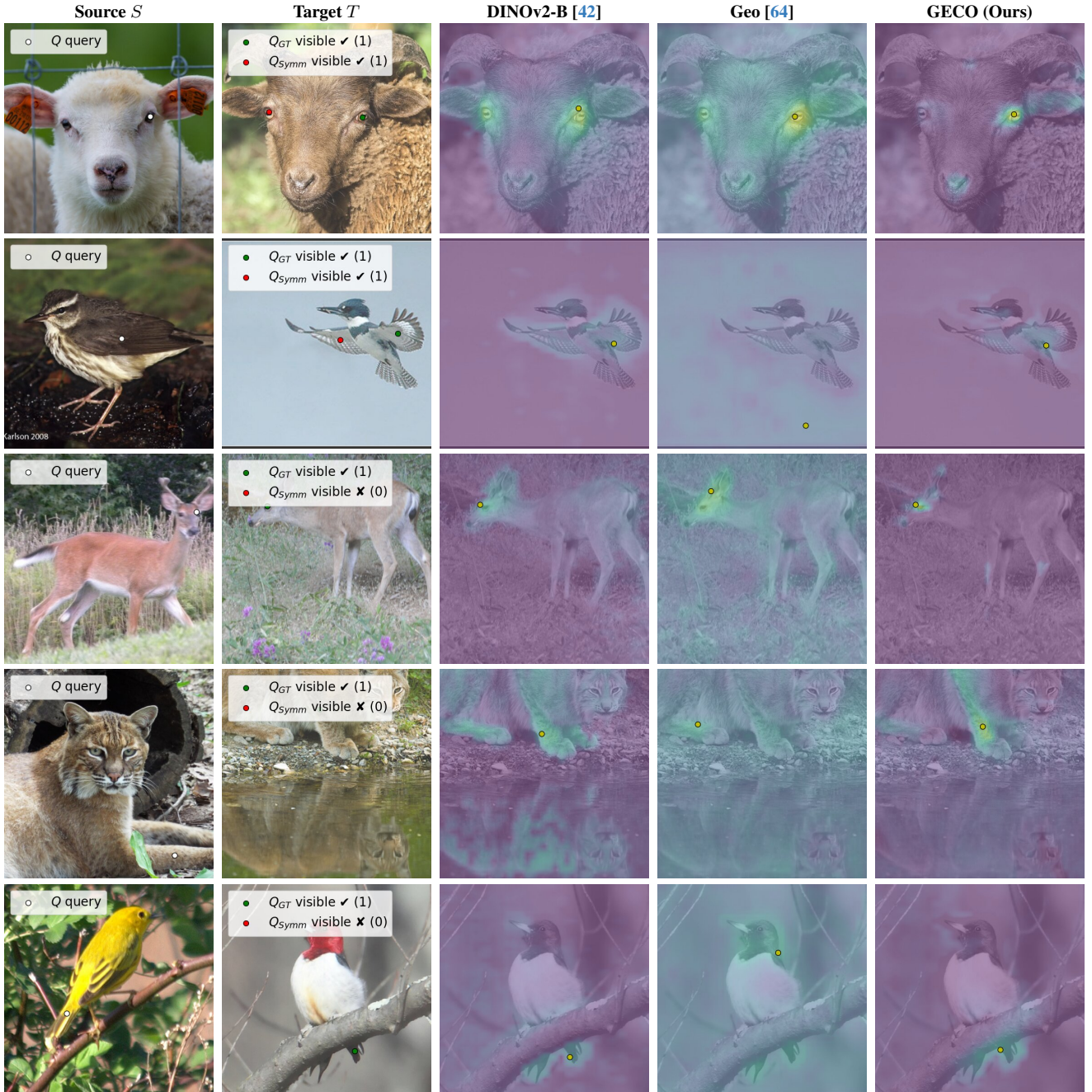


Figure 6. Qualitative results on correspondence estimation for APK [64], and CUB [55]. (Bottom row) CUB samples confirm that our method preserves the pretrained foundation model’s generalization.

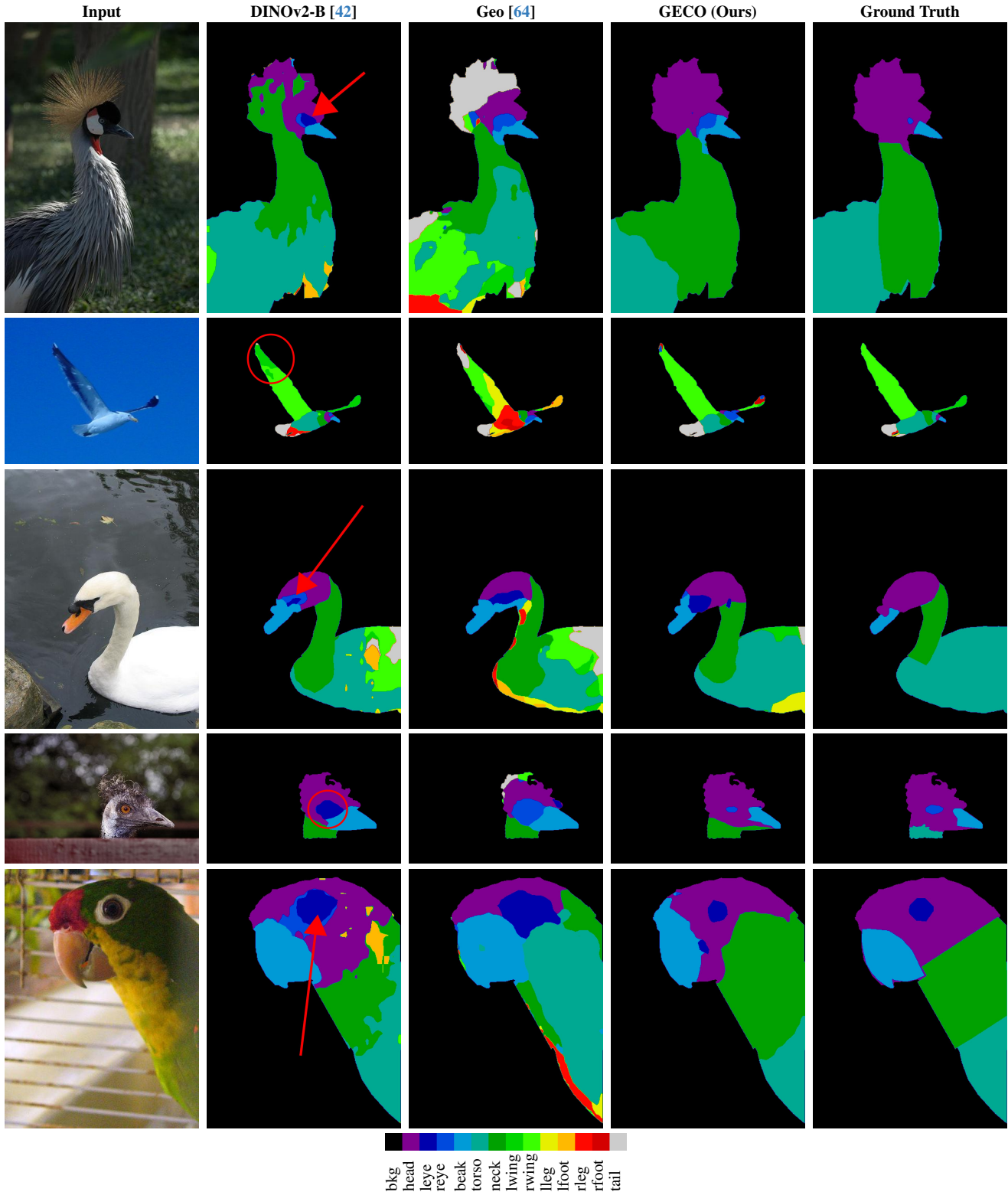


Figure 7. Clustering of the feature space based on Euclidean distance to a part representation vector for PascalParts [6]. Our learned representation effectively separates even challenging parts, such as left and right eyes, wings, and ears, while also being similarly time and memory efficient as the DINOv2v2-B backbone and much more time efficient than Geo.

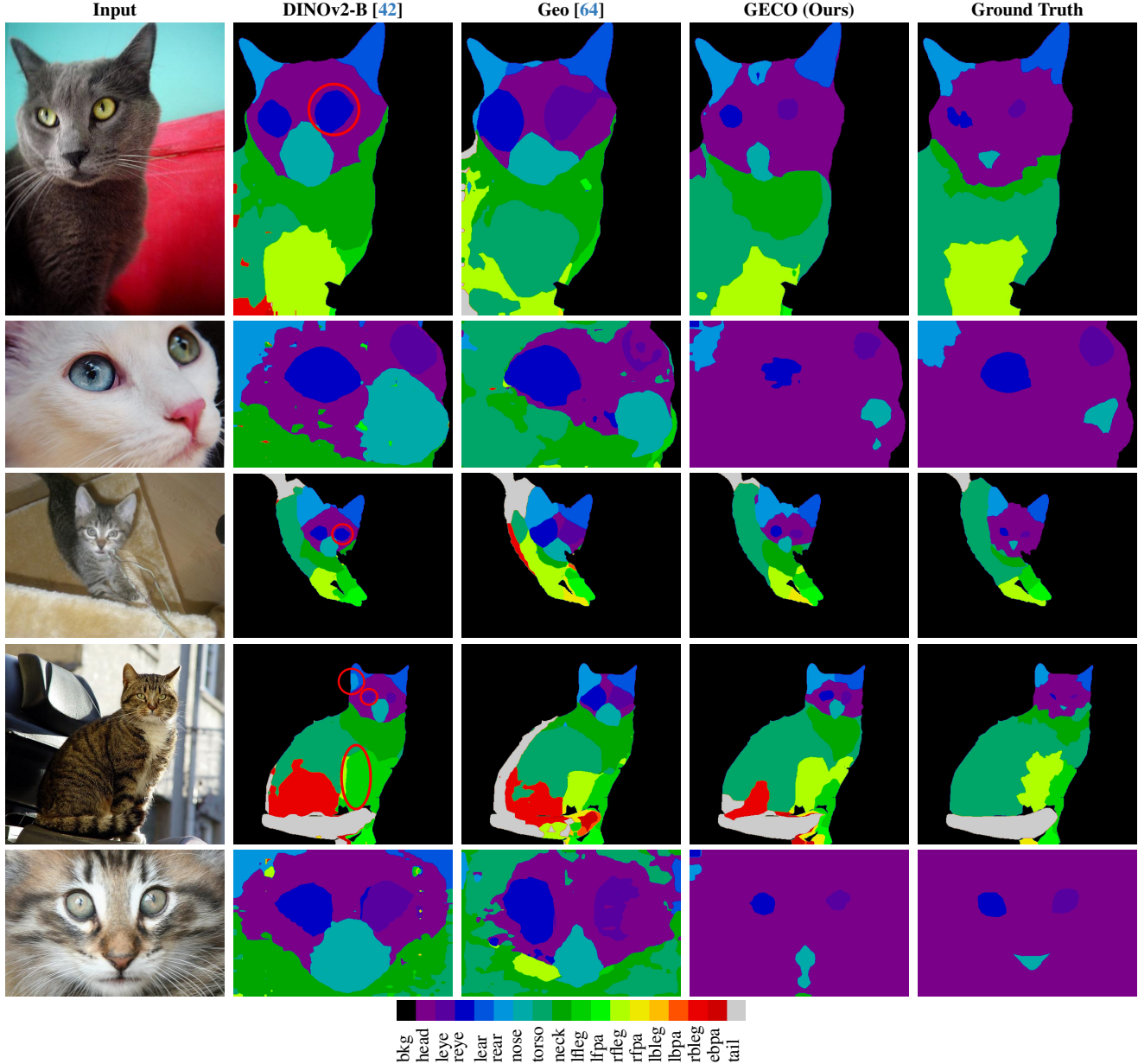


Figure 8. **Clustering of the feature space based on Euclidean distance to a part representation vector for PascalParts [6].** Our learned representation effectively separates even challenging parts, such as left and right eyes, wings, and ears, while also being similarly time and memory efficient as the DINOv2v2-B backbone and much more time efficient than Geo.

Acknowledgements: We thank the anonymous reviewers for their valuable feedback. This work was supported by the ERC Advanced Grant SIMULACRON, by the Federal Ministry for the Environment, Nature Conservation, Nuclear Safety and Consumer Protection (BMUV) through the AuSeSol-AI project (grant 67KI21007A), and by the TUM Georg Nemetschek Institute Artificial Intelligence for the Built World (GNI) through the AICC project.

References

- [1] Shir Amir, Yossi Gandelsman, Shai Bagon, and Tali Dekel. Deep vit features as dense visual descriptors. *arXiv preprint arXiv:2112.05814*, 2(3):4, 2021. [2](#)
- [2] Nicolas Bonneel and Julie Digne. A survey of optimal transport for computer graphics and computer vision. In *Computer Graphics Forum*, pages 439–460. Wiley Online Library, 2023. [3](#)
- [3] Mathilde Caron, Piotr Bojanowski, Armand Joulin, and Matthijs Douze. Deep clustering for unsupervised learning of visual features. In *ECCV*, pages 132–149, 2018. [2](#)
- [4] Mathilde Caron, Hugo Touvron, Ishan Misra, Hervé Jégou, Julien Mairal, Piotr Bojanowski, and Armand Joulin. Emerging properties in self-supervised vision transformers. In *ICCV*, 2021. [2, 6, 7, 18, 19, 21, 22, 25, 26, 27](#)
- [5] Ting Chen, Simon Kornblith, Mohammad Norouzi, and Geoffrey Hinton. A simple framework for contrastive learning of visual representations. In *ICML*, pages 1597–1607, 2020. [2](#)
- [6] Xianjie Chen, Roozbeh Mottaghi, Xiaobai Liu, Sanja Fidler, Raquel Urtasun, and Alan Yuille. Detect what you can: Detecting and representing objects using holistic models and body parts. In *CVPR*, pages 1971–1978, 2014. [7, 10, 11, 21, 22](#)
- [7] Yue Chen, Xingyu Chen, Anpei Chen, Gerard Pons-Moll, and Yuliang Xiu. Feat2gs: Probing visual foundation models with gaussian splatting. In *CVPR*, pages 6348–6361, 2025. [2](#)
- [8] Xinle Cheng, Congye Deng, Adam Harley, Yixin Zhu, and Leonidas Guibas. Zero-Shot Image Feature Consensus with Deep Functional Maps, 2024. [3](#)
- [9] Seokju Cho, Sunghwan Hong, and Seungryong Kim. Cats++: Boosting cost aggregation with convolutions and transformers. *IEEE TPAMI*, 45(6):7174–7194, 2022. [3](#)
- [10] Subhabrata Choudhury, Iro Laina, Christian Rupprecht, and Andrea Vedaldi. Unsupervised part discovery from contrastive reconstruction. *NeurIPS*, 34:28104–28118, 2021. [3](#)
- [11] Marco Cuturi. Sinkhorn distances: Lightspeed computation of optimal transport. *NeurIPS*, 2013. [2, 3](#)
- [12] Marco Cuturi and Charlotte Bunne. Tutorial on optimal transport in learning, control, and dynamical systems. <https://icml.cc/virtual/2023/tutorial/21559>, 2023. 2024-11-12. [3](#)
- [13] Daniel DeTone, Tomasz Malisiewicz, and Andrew Rabinovich. Superpoint: Self-supervised interest point detection and description. In *CVPR workshops*, pages 224–236, 2018. [2](#)
- [14] Prafulla Dhariwal and Alexander Nichol. Diffusion models beat gans on image synthesis. *NeurIPS*, 34:8780–8794, 2021. [1, 2](#)
- [15] Olaf Dünkel, Thomas Wimmer, Christian Theobalt, Christian Rupprecht, and Adam Kortylewski. Do it yourself: Learning semantic correspondence from pseudo-labels. *arXiv preprint arXiv:2506.05312*, 2025. [3](#)
- [16] Mohamed El Banani, Amit Raj, Kevins-Kokitsi Maninis, Abhishek Kar, Yuanzhen Li, Michael Rubinstein, Deqing Sun, Leonidas Guibas, Justin Johnson, and Varun Jampani. Probing the 3d awareness of visual foundation models. In *CVPR*, pages 21795–21806, 2024. [1, 2](#)
- [17] Michael Fuest, Pingchuan Ma, Ming Gui, Johannes Schusterbauer, Vincent Tao Hu, and Björn Ommer. Diffusion models and representation learning: A survey. *arXiv preprint arXiv:2407.00783*, 2024. [2](#)
- [18] Frank Fundel, Johannes Schusterbauer, Vincent Tao Hu, and Björn Ommer. Distillation of diffusion features for semantic correspondence. In *WACV*, pages 6762–6774, 2025. [3](#)
- [19] Walter Goodwin, Sagar Vaze, Ioannis Havoutis, and Ingmar Posner. Zero-shot category-level object pose estimation. In *ECCV*, pages 516–532. Springer Nature Switzerland, 2022. [2](#)
- [20] Jean-Bastien Grill, Florian Strub, Florent Altché, Corentin Tallec, Pierre Richemond, Elena Buchatskaya, Carl Doersch, Bernardo Avila Pires, Zhaohan Guo, Mohammad Gheshlaghi Azar, et al. Bootstrap your own latent-a new approach to self-supervised learning. *NeurIPS*, 33:21271–21284, 2020. [2](#)
- [21] Kamal Gupta, Varun Jampani, Carlos Esteves, Abhinav Shrivastava, Ameesh Makadia, Noah Snavely, and Abhishek Kar. Asic: Aligning sparse in-the-wild image collections. In *CVPR*, pages 4134–4145, 2023. [2](#)
- [22] Bumsub Ham, Minsu Cho, Cordelia Schmid, and Jean Ponce. Proposal flow: Semantic correspondences from object proposals. *IEEE TPAMI*, 40(7):1711–1725, 2017. [2, 6, 7, 8, 15, 16, 17, 18, 19, 20, 27](#)
- [23] Kaiming He, Haoqi Fan, Yuxin Wu, Saining Xie, and Ross Girshick. Momentum contrast for unsupervised visual representation learning. In *CVPR*, pages 9729–9738, 2020. [2](#)
- [24] Kaiming He, Xinlei Chen, Saining Xie, Yanghao Li, Piotr Dollár, and Ross Girshick. Masked autoencoders are scalable vision learners. In *CVPR*, pages 16000–16009, 2022. [2](#)
- [25] Eric Hedlin, Gopal Sharma, Shweta Mahajan, Hossam Isack, Abhishek Kar, Andrea Tagliasacchi, and Kwang Moo Yi. Unsupervised semantic correspondence using stable diffusion. *NeurIPS*, 36:8266–8279, 2023. [2](#)
- [26] Edward J Hu, Yelong Shen, Phillip Wallis, Zeyuan Allen-Zhu, Yuanzhi Li, Shean Wang, Lu Wang, Weizhu Chen, et al. Lora: Low-rank adaptation of large language models. *ICLR*, 1(2):3, 2022. [2, 3, 4, 5](#)
- [27] Shuaiyi Huang, Luyu Yang, Bo He, Songyang Zhang, Xuming He, and Abhinav Shrivastava. Learning semantic correspondence with sparse annotations. In *ECCV*, pages 267–284, 2022. [3](#)
- [28] Wei-Chih Hung, Varun Jampani, Sifei Liu, Pavlo Molchanov, Ming-Hsuan Yang, and Jan Kautz. Scops:

Self-supervised co-part segmentation. In *CVPR*, pages 869–878, 2019. 3

[29] Gabriel Ilharco, Mitchell Wortsman, Ross Wightman, Cade Gordon, Nicholas Carlini, Rohan Taori, Achal Dave, Vaishaal Shankar, Hongseok Namkoong, John Miller, et al. Openclip. Zenodo, 2021. 3

[30] Sergio Izquierdo and Javier Civera. Optimal transport aggregation for visual place recognition. In *CVPR*, pages 17658–17668, 2024. 3

[31] Mohammad Nasir Khalid, Tianhao Xie, Eugene Belilovsky, and Tiberiu Popa. Clip-mesh: Generating textured meshes from text using pretrained image-text models. In *SIGGRAPH Asia 2022 Conference Papers*, pages 1–8, 2022. 2

[32] Dominik Kloepfer, João F Henriques, and Dylan Campbell. Loco: Learning 3d location-consistent image features with a memory-efficient ranking loss. *NeurIPS*, 37:124391–124419, 2024. 3

[33] Vincent Leroy, Yohann Cabon, and Jérôme Revaud. Grounding image matching in 3d with mast3r. In *ECCV*, pages 71–91. Springer, 2024. 3

[34] Xin Li, Deng-Ping Fan, Fan Yang, Ao Luo, Hong Cheng, and Zicheng Liu. Probabilistic model distillation for semantic correspondence. In *CVPR*, pages 7505–7514, 2021. 3

[35] Ruoshi Liu, Rundi Wu, Basile Van Hoorick, Pavel Tokmakov, Sergey Zakharov, and Carl Vondrick. Zero-1-to-3: Zero-shot one image to 3d object. In *ICCV*, pages 9298–9309, 2023. 2

[36] Grace Luo, Lisa Dunlap, Dong Huk Park, Aleksander Holynski, and Trevor Darrell. Diffusion hyperfeatures: Searching through time and space for semantic correspondence. *NeurIPS*, 36, 2024. 3

[37] Octave Mariotti, Oisin Mac Aodha, and Hakan Bilen. Improving semantic correspondence with viewpoint-guided spherical maps. In *CVPR*, pages 19521–19530, 2024. 3, 7

[38] Juhong Min, Jongmin Lee, Jean Ponce, and Minsu Cho. Spair-71k: A large-scale benchmark for semantic correspondence. *arXiv preprint arXiv:1908.10543*, 2019. 5, 6, 7, 15, 16, 17, 18, 19

[39] Tom Monnier, Matthew Fisher, Alexei A Efros, and Mathieu Aubry. Share with thy neighbors: Single-view reconstruction by cross-instance consistency. In *ECCV*, pages 285–303, 2022. 2

[40] David Novotny, Diane Larlus, and Andrea Vedaldi. Anchornet: A weakly supervised network to learn geometry-sensitive features for semantic matching. In *CVPR*, pages 5277–5286, 2017. 3

[41] Nvidia. Ngc catalog 2023 tutorial 21559. https://catalog.ngc.nvidia.com/orgs/nvai/models/imagenet_nv.dinov2, 2023. 2024-11-12. 7

[42] Maxime Oquab, Timothée Darcet, Théo Moutakanni, Huy Vo, Marc Szafraniec, Vasil Khalidov, Pierre Fernandez, Daniel Haziza, Francisco Massa, Alaaeldin El-Nouby, et al. Dinov2: Learning robust visual features without supervision. *arXiv preprint arXiv:2304.07193*, 2023. 1, 2, 3, 4, 5, 6, 7, 8, 9, 10, 11, 15, 18, 19, 21, 22, 23, 25, 26, 27

[43] Ofir Pele and Michael Werman. Fast and robust earth mover’s distances. In *CVPR*, pages 460–467, 2009. 3

[44] Gabriel Peyré, Marco Cuturi, et al. Computational optimal transport: With applications to data science. *Foundations and Trends® in Machine Learning*, 11(5-6):355–607, 2019. 4, 21

[45] Qiyang Qian, Hansheng Chen, Masayoshi Tomizuka, Kurt Keutzer, Qianqian Wang, and Chenfeng Xu. Bridging viewpoint gaps: Geometric reasoning boosts semantic correspondence. In *Proceedings of the Computer Vision and Pattern Recognition Conference*, pages 11579–11589, 2025. 3

[46] A. Radford, J.W. Kim, C. Hallacy, A. Ramesh, G. Goh, S. Agarwal, G. Sastry, A. Askell, P. Mishkin, J. Clark, and G. Krueger. Learning transferable visual models from natural language supervision. In *ICML*, pages 8748–8763. PMLR, 2021. 3

[47] Robin Rombach, Andreas Blattmann, Dominik Lorenz, Patrick Esser, and Björn Ommer. High-resolution image synthesis with latent diffusion models. In *CVPR*, pages 10684–10695, 2022. 1, 2

[48] Paul-Edouard Sarlin, Daniel DeTone, Tomasz Malisiewicz, and Andrew Rabinovich. Superglue: Learning feature matching with graph neural networks. In *CVPR*, pages 4938–4947, 2020. 2, 3, 4, 16

[49] Nick Stracke, Stefan Andreas Baumann, Kolja Bauer, Frank Fundel, and Björn Ommer. CleanDIFT: Diffusion Features without Noise. In *CVPR*, pages 117–127, 2025. 2

[50] Jiaming Sun, Zehong Shen, Yuang Wang, Hujun Bao, and Xiaowei Zhou. Loftr: Detector-free local feature matching with transformers. In *CVPR*, pages 8922–8931, 2021. 2, 3, 4

[51] Luming Tang, Menglin Jia, Qianqian Wang, Cheng Perng Phoo, and Bharath Hariharan. Emergent correspondence from image diffusion. *NeurIPS*, 36:1363–1389, 2023. 2, 5, 6, 7, 18, 19, 21, 22, 25, 26, 27

[52] James Thewlis, Hakan Bilen, and Andrea Vedaldi. Unsupervised learning of object frames by dense equivariant image labelling. *NeurIPS*, 30, 2017. 3

[53] Prune Truong, Martin Danelljan, Fisher Yu, and Luc Van Gool. Probabilistic warp consistency for weakly-supervised semantic correspondences. In *CVPR*, pages 8708–8718, 2022. 3

[54] Narek Tumanyan, Omer Bar-Tal, Shai Bagon, and Tali Dekel. Splicing vit features for semantic appearance transfer. In *CVPR*, pages 10748–10757, 2022. 2

[55] Catherine Wah, Steve Branson, Peter Welinder, Pietro Perona, and Serge Belongie. The caltech-ucsd birds-200-2011 dataset, 2011. 2, 5, 6, 7, 9, 15, 16, 17, 18, 19, 20, 25, 26, 27

[56] Jianyuan Wang, Minghao Chen, Nikita Karaev, Andrea Vedaldi, Christian Rupprecht, and David Novotny. Vggt: Visual geometry grounded transformer. In *CVPR*, pages 5294–5306, 2025. 3

[57] Shuzhe Wang, Vincent Leroy, Yohann Cabon, Boris Chidlovskii, and Jerome Revaud. Dust3r: Geometric 3d vision made easy. In *CVPR*, pages 20697–20709, 2024. 3

[58] Yuanbo Xiangli, Ruojin Cai, Hanyu Chen, Jeffrey Byrne, and Noah Snavely. Doppelgangers++: Improved Visual Disambiguation with Geometric 3D Features. In *CVPR*, pages 27166–27175, 2025. 3

- [59] Jiankai Xing, Fujun Luan, Ling-Qi Yan, Xuejun Hu, Houde Qian, and Kun Xu. Differentiable rendering using rgbxy derivatives and optimal transport. *ACM Transactions on Graphics (TOG)*, 41(6):1–13, 2022. 3
- [60] Chenfeng Xu, Huan Ling, Sanja Fidler, and Or Litany. 3difftection: 3d object detection with geometry-aware diffusion features. In *CVPR*, pages 10617–10627, 2024. 3
- [61] Fei Xue, Sven Elflein, Laura Leal-Taixe, and Qunjie Zhou. MATCHA: Towards Matching Anything. In *CVPR*, pages 27081–27091, 2025. 3
- [62] Jianing Yang, Alexander Sax, Kevin J. Liang, Mikael Henaff, Hao Tang, Ang Cao, Joyce Chai, Franziska Meier, and Matt Feiszli. Fast3r: Towards 3d reconstruction of 1000+ images in one forward pass. In *CVPR*, pages 21924–21935, 2025. 3
- [63] Yuanwen Yue, Anurag Das, Francis Engelmann, Siyu Tang, and Jan Eric Lenssen. Improving 2d feature representations by 3d-aware fine-tuning. In *ECCV*, pages 57–74, 2024. 3
- [64] Junyi Zhang, Charles Herrmann, Junhwa Hur, Eric Chen, Varun Jampani, Deqing Sun, and Ming-Hsuan Yang. Telling left from right: Identifying geometry-aware semantic correspondence. In *CVPR*, pages 3076–3085, 2024. 1, 2, 3, 6, 7, 8, 9, 10, 11, 15, 16, 17, 18, 19, 20, 21, 22, 23, 25, 26, 27
- [65] Junyi Zhang, Charles Herrmann, Junhwa Hur, Luisa Polanía Cabrera, Varun Jampani, Deqing Sun, and Ming-Hsuan Yang. A tale of two features: Stable diffusion complements dino for zero-shot semantic correspondence. *NeurIPS*, 36, 2024. 2
- [66] Jinghao Zhou, Chen Wei, Huiyu Wang, Wei Shen, Cihang Xie, Alan Yuille, and Tao Kong. ibot: Image bert pre-training with online tokenizer. *arXiv preprint arXiv:2111.07832*, 2021. 2

GECO: Geometrically Consistent Embedding with Lightspeed Inference

Supplementary Material

Contents

| | |
|---------------------------------------|-----------|
| 1. Introduction | 1 |
| 2. Related Work | 2 |
| 3. Background | 3 |
| 4. Method | 4 |
| 5. Experiments | 4 |
| 5.1. Analysis with (and of) PCK | 5 |
| 5.1.1. Evaluation | 6 |
| 5.2. Feature Space Segmentation | 7 |
| 5.2.1. Evaluation | 7 |
| 5.3. Runtime | 7 |
| 6. Conclusion | 7 |
| 7. Implementation Details | 15 |
| 7.1. Architecture Details | 15 |
| 7.2. Training Details | 15 |
| 7.3. Loss Function | 16 |
| 7.4. Ablation Study on Design Choices | 16 |
| 8. Additional Experiments | 17 |
| 8.1. Analysis with (and of) PCK | 17 |
| 8.2. Feature Space Segmentation | 21 |
| 8.3. 2D-3D Matching | 23 |

7. Implementation Details

7.1. Architecture Details

Feature Encoder Hyperparameters We identified notable differences in the optimal settings for DINOv2 and DINO that are not explicitly documented in their original papers. For DINOv2, we achieve the best performance by using patch tokens from the final transformer layer, particularly when working with higher-resolution images. In contrast, DINO performs better when using patch tokens from the fourth-to-last transformer layer, with optimal results at an input resolution of 244; performance degrades with higher resolutions.

Based on these findings, we use the DINOv2 backbone [42] with an input resolution of 518 and patch tokens from the final transformer layer in our model.

Architecture We learn low-rank matrices (rank 10) for each attention layer, which are added to the 768×768 -dimensional weight matrices of the linear layers before being passed to the attention mechanism ($768 \times 10 \times 2$ parameters). For DINOv2-B, this results in $v = 768 \times 10 \times 2 \times 12 \times 2$ parameters, with a depth of 12 and updating query and value matrices equating $v \times 4$ bytes (≈ 1.4 MB) of learnable parameters. This is significantly fewer than the 19 MB of learnable parameters introduced by Geo [64]. This small parameter count and simple architecture enable us to increase the inference time of DINOv2-B by less than 1 millisecond.

7.2. Training Details

Training Hyperparameters The models are trained using the Adam optimizer with a learning rate of 0.0001, no weight decay, and no learning rate scheduler, with a batch size of 6. A key advantage of our approach is the ability to train directly on raw images without preprocessing, which allows for increased data augmentation and larger batch sizes. Training is conducted on a single GPU for 8 epochs. For the loss functions, weights are set as follows: 1 for the positive loss, 1 for the bin loss, and 10 for the negative loss.

Dataset Shuffling Training is conducted jointly across the PFPascal, SPair [38], and APK [64] datasets. We employ a reweighting scheme that samples up to 800 examples per category. We found this hyperparameter by trading off the validation accuracies for the different datasets (see Sec. 7.4). In fact, if one dataset dominates the training, the model tends to overfit to that dataset.

Image Pair Augmentation We leverage existing datasets [22, 38, 55, 64] containing images of diverse category instances with varying shapes, textures, and motion deformations, captured under different lighting and camera setups. Thanks to our method’s low computational cost, we use more data augmentation than [64] to improve generalization. We incorporate flipping, cropping, and color jitter into the augmentation pipeline, generating more positive, negative, and bin pairs for feature matching (see Fig. 2). Specifically, flipping creates challenging positive/negative pairs, while cropping increases bin pairs by promoting matches to the bin rather than to semantically similar but geometrically inconsistent features.

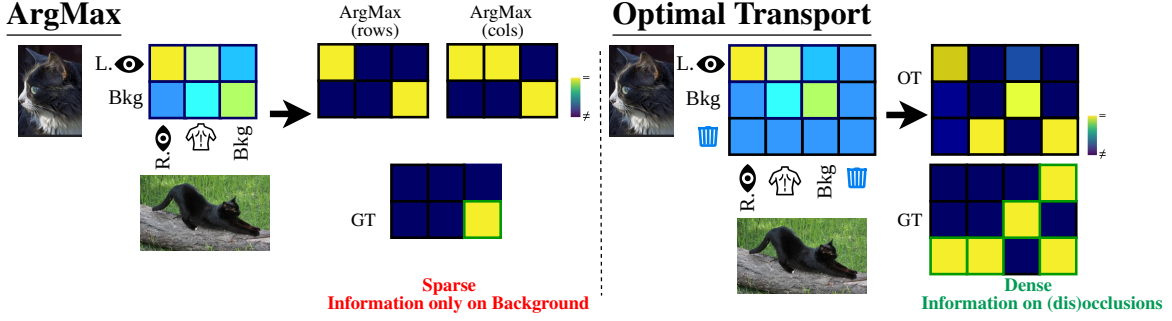


Figure 9. **Intuition on OT and geometry.** Standard ArgMax loss (left) provides positive supervision only for elements that appear in both images. Optimal Transport (right) uses the bin to provide explicit signals also on elements that appear in only one of the images. This is particularly common for non-rigid shapes (e.g., animals), as often a point and its symmetrical counterpart (e.g., left and right eyes) face (dis)occlusions. Intuitively, this leads to a stronger signal for learning features that better disambiguate symmetries.

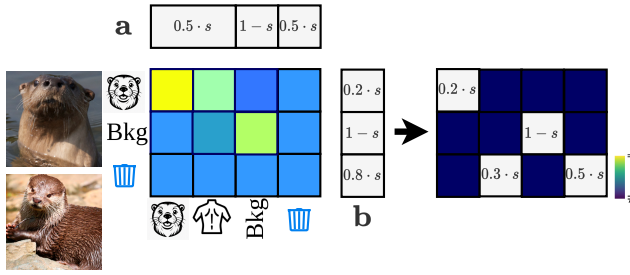


Figure 10. **Optimal Transport Marginals.** This figure illustrates the marginal distribution used in the Optimal Transport algorithm, assigning s to the shape and $1 - s$ to the background. The visible content proportion is estimated from keypoint annotations by calculating the ratio of visible to total keypoints. In this example, the top image has a visibility ratio of 0.2 (only the head is visible), while the bottom image has a ratio of 0.5 (the head and one side of the body are visible) relative to the full shape.

7.3. Loss Function

Motivation for OT We argue that Optimal Transport (OT) provides stronger geometric supervision than Argmax, as shown in Fig. 9. As already pointed out in Sec. 3 there are several drawbacks when using Argmax to construct a loss function. Here, we highlight, that OT incorporates the supervision signal of points, visible in only one image, which often occurs with symmetric parts of non-rigid objects (e.g., eyes) by introducing a dustbin entry in the assignment matrix. Furthermore, due to the interaction between features, the OT loss enables to densely backpropagate the gradient. For example, a bin assignment signal pushes down the similarity to all other features, which is not possible with Argmax.

Designing marginal distributions Since correspondence data is valuable, a key contribution of our work is using it to construct marginal distributions see Fig. 10. To define the marginals for the Optimal Transport (OT) problem, we depart from the conventional approach, employed in Super-

| | PFPPascal [22] | APK [64] | Spair [38] | CUB [55] |
|---------------|----------------|-------------|-------------|-------------|
| GECO (Ours)-S | 89.6 | 83.4 | 78.0 | 90.4 |
| GECO (Ours) | 92.1 | 86.7 | 85.2 | 92.5 |

Table 3. **Impact of model size on performance (PCK \uparrow).** Comparison of our approach using DINOv2-B and DINOv2-S backbones on PFPPascal [22], CUB [55], Spair [38], and APK [64] datasets. The results indicate that model size plays a crucial role in overall performance.

Glue [48], which assigns 0.9 to the image and 0.1 to the bin. Instead, we utilize automatically generated mask annotations to distinguish between foreground and background, leveraging an off-the-shelf segmentation tool [67].

In our formulation, the shape mass is assigned a value of $s = 0.9$, with the remaining $1 - s$ allocated to the background, as illustrated in Fig. 10. The proportion of visible content, denoted as x , is estimated by calculating the ratio of visible keypoints to the total number of keypoints. This leads to $x \cdot s$ being assigned to the foreground and $(1 - x) \cdot s$ to the bin.

This marginal distribution, together with the padded cosine similarity matrix of the features, is then fed into the Optimal Transport algorithm to determine the optimal transport plan.

7.4. Ablation Study on Design Choices

Impact of model size on performance (PCK) When scaling down the architecture to DINOv2-S, we observe a decline in performance, which we attribute to the reduced capacity of the model. While it still captures geometric relationships between keypoints, its performance does not match that of the larger variant, as shown in Tab. 3.

Impact of the Optimal Transport Marginals We evaluate the impact of the marginal distribution on the performance of our method. We compare the standard marginals used in SuperGlue [48] with our approach, which leverages mask annotations to distinguish between foreground

| | PFPascal [22] | APK [64] | SPair [38] | CUB [55] |
|---------------|---------------|-------------|-------------|-------------|
| GECO (Ours)-N | 91.5 | 86.0 | 83.7 | 89.5 |
| GECO (Ours) | 92.1 | 86.7 | 85.2 | 92.5 |

Table 4. **Impact of choice of marginals on performance (PCK \uparrow).** We evaluate the effect of incorporating more sophisticated marginals (Bottom row) in the loss function compared to the standard formulation (Top row). Our results show that while the performance difference on the test splits of APK, PFPascal, and SPair remains within a margin of 1.5, the performance drop on the generalization task is substantially larger, reaching a value of 3. This highlights the importance of incorporating improved marginals for better generalization.

| | mean mIoU \uparrow | mean Acc \uparrow |
|----------------------|----------------------|---------------------|
| GECO (Ours) (w/o KL) | 36.4 | 88.5 |
| GECO (Ours) | 37.9 | 89.0 |

Table 5. **Impact of choice of marginals on performance (Segmentation Accuracy).** We evaluate using the segmentation metrics explained in Sec. 8.2. We show the effect of incorporating the KL-marginal regularization (Bottom row) in the loss function compared to the standard formulation with hard constraints on the marginal distributions (Top row).

and background. We found that our approach outperforms the standard marginals especially on the generalization to the CUB [55] dataset, as shown in Tab. 4.

Impact of the KL Divergence Regularization on the marginals The benefit of KL regularization is clear in the segmentation results, as shown in Tab. 5. Because the estimated marginals are imperfect, KL reduces overfitting to noise during training and should be increased when exact marginals are available (e.g., images rendered from 3D shapes).

Impact of dataset shuffling on the performance We evaluate the effect of dataset shuffling on performance across different datasets. As our method is trained jointly on SPair [38], PFPascal [22], and APK [64], shuffling enables better generalization. To address category imbalance, we sample up to K image pairs per category; if fewer are available, all are used.

Performance is highly sensitive to the choice of K . Low values (e.g., 100-400) lead to overfitting on PFPascal and poor generalization to SPair and CUB. Conversely, high K underrepresents PFPascal, limiting its validation accuracy. We find that $K = 800$ yields the best overall performance.

8. Additional Experiments

We provide more detailed experiments to analyze the PCK metric and its subsets in Sec. 8.1. In Sec. 8.2, we complement the qualitative analysis of the segmentation performance in the main paper with a quantitative and qualitative evaluation of the segmentation confusion matrix. In Sec. 8.3, we provide an additional experiment focusing on rigid shapes with diverse appearances and demonstrate our methods performance on keypoint matching by evaluating 2D-3D projections.

8.1. Analysis with (and of) PCK

Influence of different radii on unambiguous True Positives A critical choice of PCK is the radius in which a prediction is considered correct. This also has an impact on our PGCK subdivision. Here, we investigate how the choice of the PCK metric’s radius influences the unambiguous true positive subset’s cardinality (see Fig. 11). As expected, the unambiguous correct predictions decrease with the radius, while the overall PCK increases (see Fig. 12). For larger radius values, the PCK metric reflects the model’s ability to identify general correspondences across the image, even when semantic parts are widely distributed rather than concentrated in a single area. In contrast, for smaller radius values, the metric emphasizes the model’s precision in pinpointing correspondences with high spatial accuracy and its ability to distinguish between closely spaced keypoints, such as those on the left and right sides, when both are present.

Results In the main paper, we reported the subsets of the PGCK for one value of Fig. 11 on APK [64]. Here, we extend this analysis to the CUB [55] and SPair [38] datasets. As shown in Fig. 11a, our method achieves a slight improvement over previous work in unambiguous correct predictions on the CUB [55] dataset. For the APK [64] and SPair [38] datasets, performance varies: our method outperforms the competitor in one case, while in the other, the competitor demonstrates a more refined geometric understanding. These results suggest that geometric understanding is dataset-dependent.

Additionally, given the performance drop on CUB observed in competing methods on the semantic understanding task (see Fig. 12c), we argue that our approach strikes a favorable balance between geometric and semantic understanding. Unlike the competitors, our method preserves previously learned properties, making it a more robust and well-rounded solution. Moreover, it remains competitive with the state of the art while significantly reducing memory consumption and runtime from 2274 ms to 43 ms.

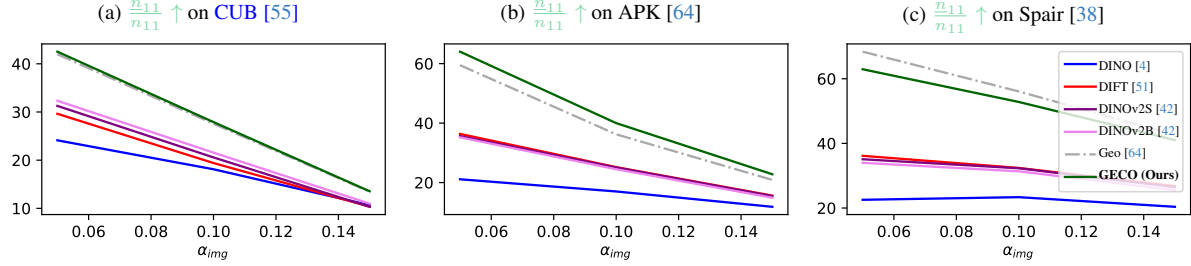


Figure 11. **Geometric ambiguity as a function of radius.** As the radius decreases, the set of unambiguous true positives $\frac{n_{11}}{n_{11}}$ grows, where the target keypoint is outside the radius of any incorrect matches. This figure illustrates the PGCK subset, specifically the unambiguous correct predictions, for various radius values (@ α_{img}) on CUB [55], APK [64], and Spair [38]. Our method outperforms previous work on two out of three datasets while achieving a reduction in runtime and memory usage by two orders of magnitude.

Influence of different radii on PCK As expected the PCK values are increasing with varying radius. It measures the general semantic knowledge of features with a part also measuring the geometric understanding.

Results We present detailed results, evaluated on the PF-Pascal [22], APK [64], SPair [38], and CUB [55] datasets. Specifically, in Fig. 12 we show the PCK values for different radii across these datasets. Notably, our method significantly outperforms the current state-of-the-art on three out of the four datasets, highlighting the superior effectiveness of our approach. While the competitor Geo [64] achieves comparable performance to ours in geometric understanding on the generalization task to CUB [55] (see Fig. 11a), we observe significant catastrophic forgetting in the n_{10} and n_{1x} splits leading to worse overall results than DINOv2-S (see Fig. 12c). In contrast, our method maintains consistent performance across all splits and outperforms Geo [64] in three out of four cases, demonstrating its robustness and reliability.

Qualitative results We illustrate various failure modes of existing approaches and demonstrate how our method addresses these issues. In Fig. 13, we show that our method can correctly assign a keypoint to the bin even when the actual match is occluded. This ability is learned through bin and negative losses, which encourage the assignment to the bin rather than to the symmetric counterpart. When the match is occluded, the model becomes better calibrated, generating minimal attention on the target image, including the symmetric counterpart. This represents a failure mode that the PCK metric does not capture, as the symmetric counterpart is absent in the target image, and consequently, this keypoint pair is excluded from the PCK evaluation.

We also report performance on the geometrically relevant case, where multiple semantically similar keypoints are present in the target image. In this scenario, our method is more confident in the predictions, focusing only on the rel-

| CUB [55] | | | | | | | | | |
|------------|-----|-----|-----|-----|-----|-----|-----|-----|--|
| SPair [38] | | | | | | | | | |
| Aer | Bik | Bir | Boa | Bot | Bus | Car | Cat | Cha | |
| 34 | 53 | 23 | 30 | 97 | 43 | 40 | 82 | 81 | |
| Cow | Dog | Hor | Mot | Per | Pla | She | Tra | TV | |
| 80 | 46 | 61 | 69 | 34 | 73 | 72 | 90 | 62 | |
| APK [38] | | | | | | | | | |
| alo | ant | arg | bea | bis | bla | bob | bro | buf | |
| 37 | 31 | 28 | 21 | 20 | 32 | 36 | 33 | 34 | |
| cat | che | chi | cow | dee | dog | ele | fox | gir | |
| 42 | 30 | 37 | 38 | 36 | 36 | 36 | 33 | 24 | |
| gor | ham | hip | hor | jag | kin | leo | lio | mar | |
| 42 | 34 | 40 | 26 | 32 | 33 | 40 | 40 | 27 | |
| mon | moo | mou | noi | ott | pan | pan | pig | pol | |
| 37 | 24 | 20 | 38 | 28 | 23 | 46 | 35 | 30 | |
| rab | rac | rat | rhi | she | sku | sno | spi | squ | |
| 7 | 28 | 27 | 23 | 34 | 19 | 35 | 35 | 16 | |
| tig | uak | wea | wol | zeb | | | | | |
| 32 | 39 | 36 | 34 | 24 | | | | | |

Table 6. **PGCK Dataset imbalance.** Completing Fig. 3, we report the geometric aware n_{11}/n_{11} counts only the pairs for which a geometric mismatch is possible. Categories often present high imbalance, and geometrical error modes would have a different weight.

event areas of the image (see Fig. 14). As shown in Fig. 15, our features localize keypoints precisely in the target image without spreading similarity across irrelevant regions.

PGCK Dataset imbalance We analyze the cardinality of the geometrically aware subset in Fig. 3, which is able to assess the confusion between keypoints on opposite sides of the symmetry axis. To complete the table for all categories, we present a detailed report for the CUB [55], SPair [38], and APK [64] datasets in Tab. 6.

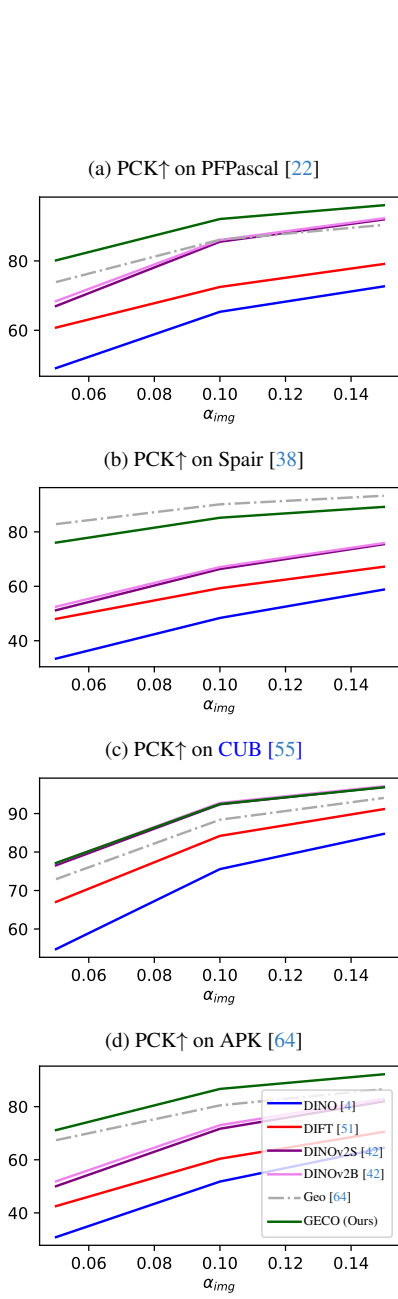


Figure 12. **PCK as a function of radius.** As the radius decreases, the set of correct matches declines. This figure illustrates the PCK metric for various radius values ($@\alpha_{img}$) on CUB [55], APK [64], and Spair [38]. Our method outperforms previous work on three out of four datasets while achieving a reduction in runtime and memory usage by two orders of magnitude.

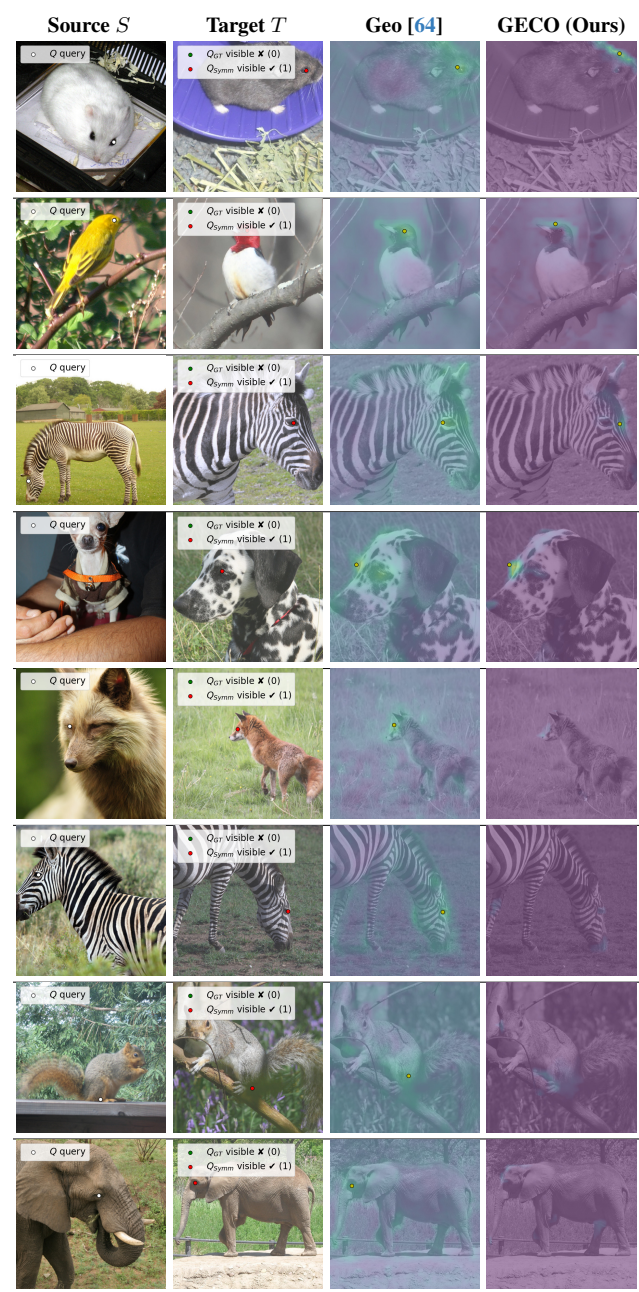


Figure 13. **Qualitative results on the task of assignment to the bin (01-case) on APK [64] and CUB [55] (fifth row).** We show that our method predicts small cosine similarities, if the actual match is occluded. This is learned by the bin and negative losses, which encourage the assignment to the bin instead of the symmetric counterpart. (First five rows) It is clearly visible, that the model knows the location of the ground truth correspondence, which could become visible by a small movement. The location of the symmetric counterpart is ignored. (Last three rows) We receive only low attention values for the whole image, including the symmetric counterpart, when the symmetric counterpart is occluded.



Figure 14. **Qualitative results on the task of assignment to the correct correspondence (11-case) on PFPascal [22] (First five rows), APK [64] (In the middle) and CUB [55] (Last row).** In the samples above the symmetric counterpart is visible in the target view. While previous work assigns attention on most of the image, our model is more confident in the predictions and only attends to the regions of interest.

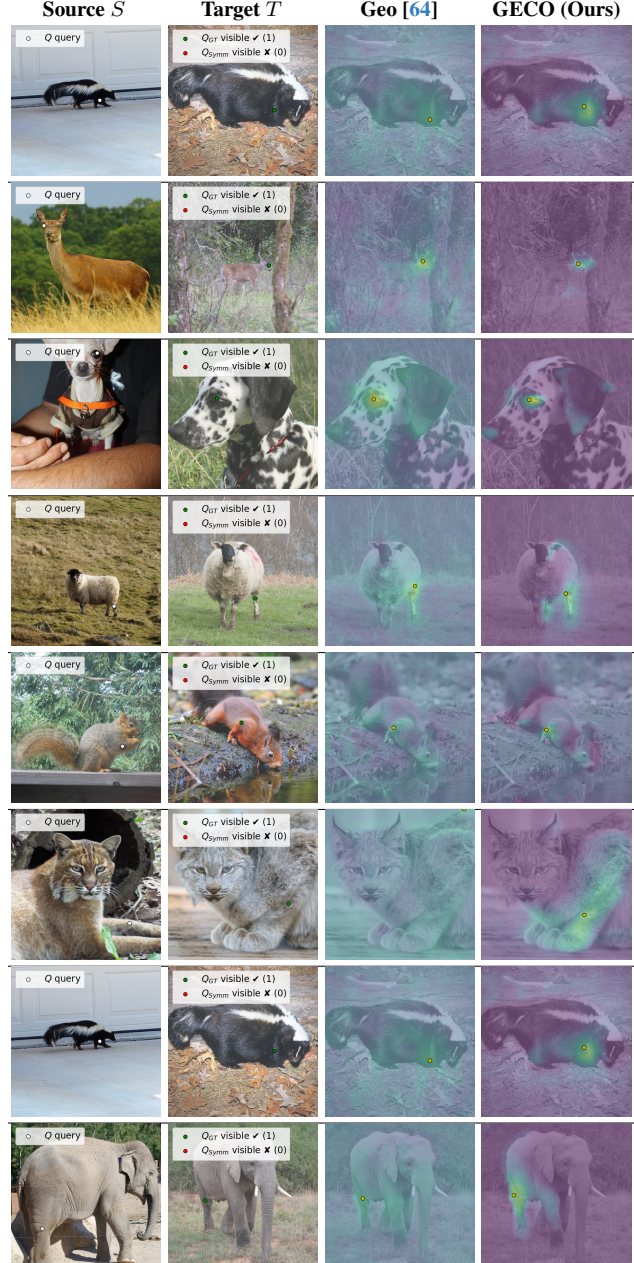


Figure 15. **Qualitative results on the task of semantic correspondence estimation (10-case) on APK [64] and CUB [55] (Last row).** In the above samples only one semantically similar keypoint is visible in the target view. While previous work assigns attention on most of the image, our model is more confident in the predictions and only attends to the regions of interest.

8.2. Feature Space Segmentation

In Sec. 5.2, we revisit the procedure for evaluating the separability of the feature space by leveraging annotated parts and computing centroids for each. To complement the qualitative analysis, we now present a quantitative evaluation using standard segmentation metrics. Furthermore, we include normalized confusion matrices for another qualitative analysis to highlight the geometric consistency of the predicted segmentations.

Dataset We use the PascalParts [6] dataset, which offers detailed part annotations for a wide variety of object categories, enabling consistent and comprehensive evaluation across different classes. However, some of the 20 categories, such as *boat*, *table*, and *sofa*, have only a single part annotated. As a result, we exclude these categories from our evaluation.

Evaluation Similar to prior work [44][68] we use the **accuracy** and **mean Intersection over Union (mIoU)** as our primary evaluation metrics. To compute these metrics, let s_{ij} represent the number of patches from ground-truth part i that are predicted as part j by the model.

The mean Intersection over Union (mIoU) is defined as

$$\text{mIoU} = \frac{1}{N} \sum_i \frac{s_{ii}}{\sum_j s_{ij} + \sum_j s_{ji} - s_{ii}}, \quad (12)$$

where N is the number of parts. The accuracy is defined as:

$$\text{Acc} = \frac{\sum_i s_{ii}}{\sum_i \sum_j s_{ij}}. \quad (13)$$

This approach provides a per-category measure, enabling a detailed comparison of part segmentation performance across different parts. For an overall evaluation, we compute the average metric across all categories.

In addition, we report metrics specifically for the geometric subdivision, which includes parts divided into left and right counterparts, such as *legs*, *wings*, *eyes*. The geometric subdivision is presented both quantitatively and qualitatively through a confusion matrix. This focused analysis allows us to assess the model’s ability to distinguish symmetric parts, which is critical for understanding its geometric reasoning capabilities.

Results In Tab. 7, we report the average mIoU and average accuracy across categories, evaluating performance on the segmentation task using the PascalParts [6] dataset.

First, evaluating all parts within each category on the left side of Tab. 7, offers insight into the model’s capacity to differentiate between parts that are not necessarily symmetric, such as *head*, *body*, and *tail*. Although accuracy remains

| | mean mIoU↑ | mean Acc↑ | mean mIoU↑ | mean Acc↑ |
|--------------------------|-------------|-------------|-------------|-------------|
| | (geo) | (geo) | (geo) | (geo) |
| DINO [4] | 31.5 | 87.9 | 44.1 | 95.9 |
| DIFT _{adm} [51] | 31.5 | 87.9 | 48.0 | 96.4 |
| DINOv2B [42] | 39.8 | 90.1 | 57.6 | 97.3 |
| Geo [64] | 37.1 | 88.4 | 62.8 | 97.6 |
| GECO (Ours) | <u>37.9</u> | <u>89.0</u> | <u>63.0</u> | <u>97.5</u> |

Table 7. **Quantitative Evaluation of Segmentation Confusion Matrices on PascalParts [6].** Our features retain the segmentation performance of DINOv2 (two left columns), while additionally enabling the distinction between left and right parts (right two columns). The best scores are shown in **bold** and the second best are underlined. Methods with a performance difference of less than 0.5% are considered to be on par.

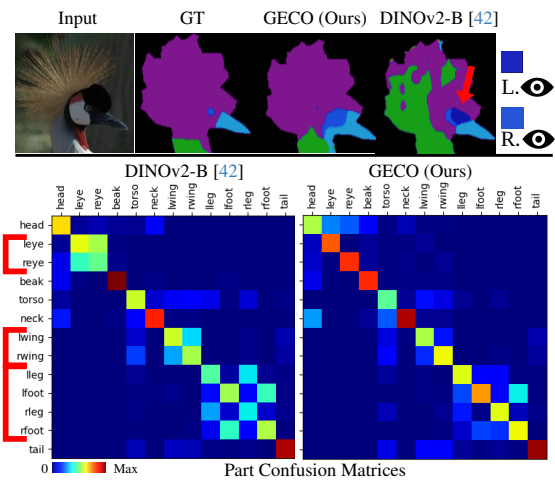


Figure 16. **Results on Symmetry.** **Top:** Our method reduces symmetric mismatches in part clustering. **Bottom:** We show the part confusion matrix (patches aggregated for each part across images), highlighting geometric confusion (red brackets).

high across methods, mIoU scores decline due to sensitivity to class imbalance in the parts. Both fine-tuned geometry aware methods (last two rows) perform worse on non geometric parts, as expected. However, our method outperforms Geo [64], indicating better retention of non geometric information.

On the right side of Tab. 7, we report the metrics for the geometric parts only. As expected, both geometry-aware methods outperform all foundation models. The connection between the qualitative part segmentation results in Fig. 7 and the confusion matrix analysis is demonstrated in Fig. 16. Visual inspection aligns with the numbers and reveals that DINOv2-B struggles with symmetric distinctions (e.g., left vs. right). Additional examples of checkerboard patterns indicative of geometric confusion are shown in Fig. 17. Here, the matrices contain only geometrically confusable parts and are normalized to mitigate class imbalance.

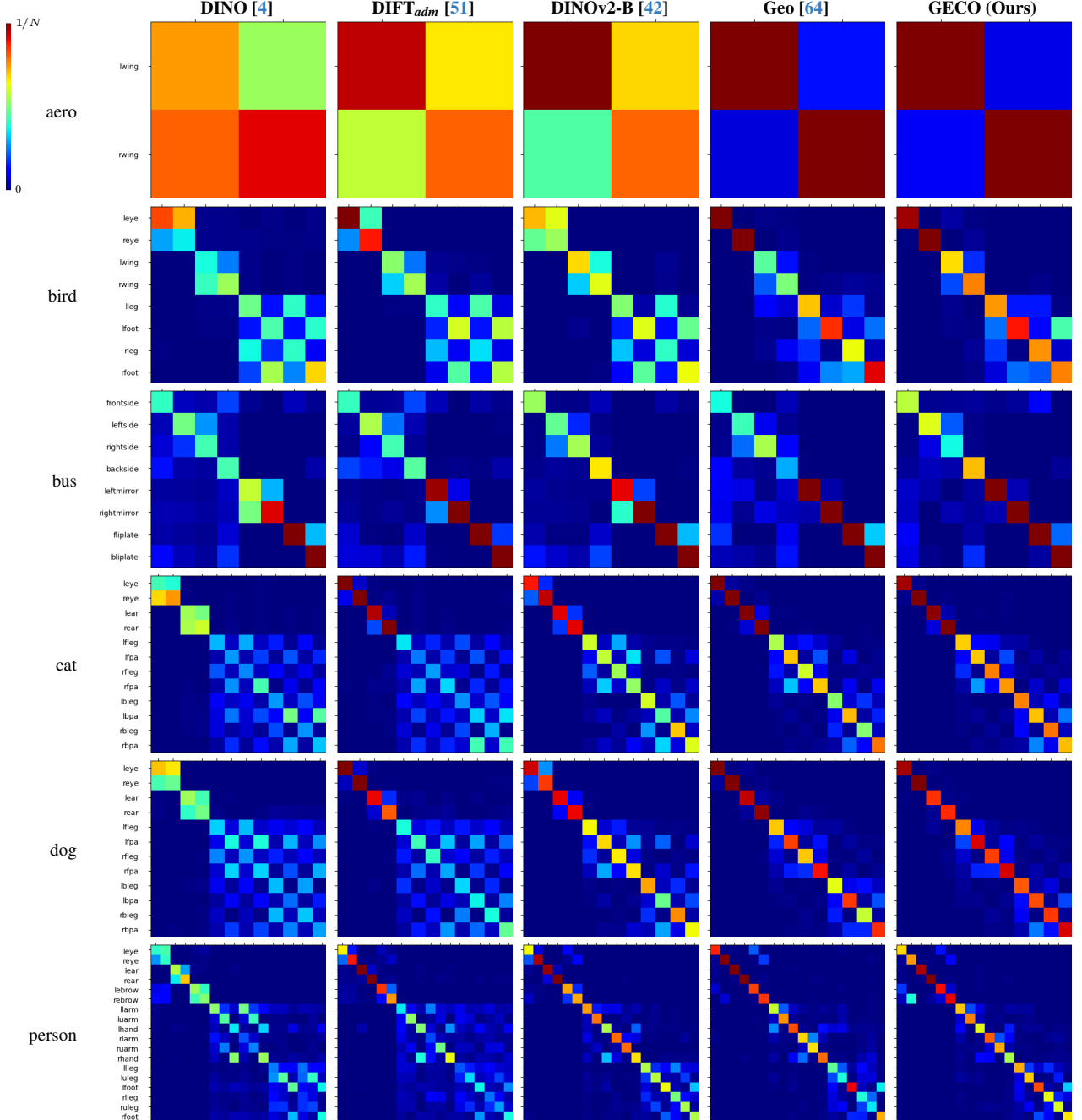


Figure 17. Qualitative Evaluation of Segmentation Confusion Matrices on PascalParts [6]. We present the confusion matrix for the segmentation task on the PascalParts [6] dataset, showing every second category in alphabetical order. The matrix displays predicted parts on vertical and ground truth parts on the horizontal axis, plotting only parts per category with annotated symmetrical counterparts for visualization purposes. Diagonal entries indicate correct predictions, while off-diagonal entries show misclassifications. To address class imbalance, the matrix is column-normalized: each column is divided by the total number of patches for that ground truth part. With number of parts N , each ground truth part annotation is assigned a total mass of $1/N$, which is distributed across the predicted parts, such that the columns sum to $1/N$. The colour coding depends on the number of parts N .

8.3. 2D-3D Matching

Structure-from-Motion (SfM), Perspective-n-Point (PnP), and related methods that rely on rigid geometry are not typical applications of non-rigid intra-category feature learning, which remains effective even under substantial intra-class variations in shape and appearance. Nevertheless, we demonstrate that our features support downstream tasks such as inter-instance 2D-3D alignment, which is essential for pose estimation and geometric reasoning.

Dataset To obtain data that combines intra-class variability with rigid structure, we render two 3D animal meshes from the SMAL model [69]. We enhance their realism and intra-class diversity using ControlNet (see Fig. 18, Top), and j filter out hallucinated outputs.

Procedure We decorate all mesh vertices with our features by median-aggregating across views, using the ground-truth camera poses (see Fig. 18, Top). For 20 novel images, we compute 2D-3D correspondences (see Fig. 18, Bottom) using argmax matching to the mesh vertex with the highest feature similarity.

We report the mean geodesic distance between matched 2D keypoints (unprojected onto the mesh) p and ground-truth vertex p_{gt} :

$$\bar{d}_{geo} = \text{mean} (d_{geo}(p, p_{gt})) , \quad (14)$$

where d_{geo} denotes the shortest path along the mesh surface between two vertices. In Fig. 18 (Bottom), black contours indicate regions of high geodesic error, where the matched 3D vertex is distant from the ground truth.

We further evaluate camera pose estimation based on these 2D-3D matches. A robust PnP algorithm inside RANSAC estimates the camera’s rotation and translation relative to the 3D object. The quality of the estimated rotation R is assessed by comparing it to the ground-truth rotation R_{gt} using the median rotation error across all images:

$$\bar{e}_{rot} = \text{median} \left(\arccos \left(\frac{\text{trace}(Rgt^T R) - 1}{2} \right) \right) . \quad (15)$$

Results As shown in Tab. 8, our GECO features outperform both Geo [64] and DINOv2-B [42] in terms of rotation error and geodesic distance. This confirms that our method enables effective intra-category 2D-3D matching for pose estimation and geometric reasoning.

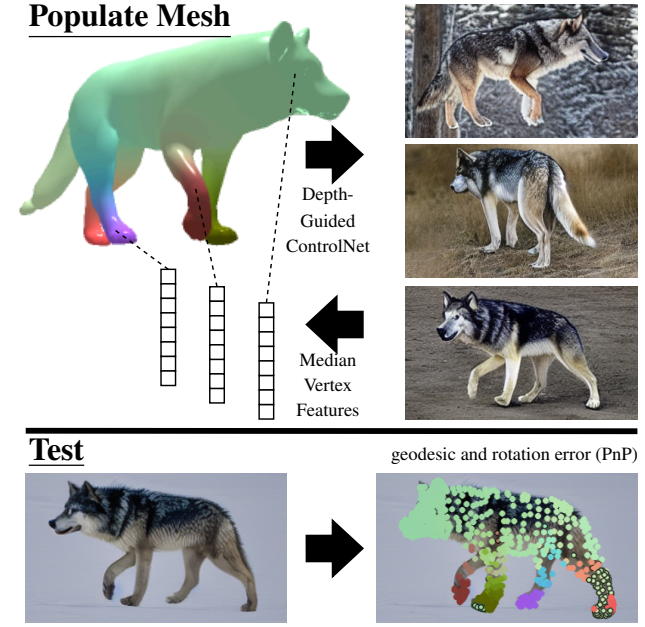


Figure 18. **Evaluation Protocol.** **Top:** A mesh from the SMAL model [69] is rendered to obtain depth images, which guide ControlNet-based synthesis of realistic 2D images. Hallucinated outputs are manually filtered. Mesh vertices are then populated with features by taking the median across the corresponding 2D views. **Bottom:** A novel view is processed, and 2D-3D correspondences are established via argmax matching to the mesh vertex with the highest feature similarity. Matches are color-coded according to surface color. Those exceeding a geodesic distance threshold d_{geo} to the ground-truth location are highlighted with a black contour.

| | $\bar{e}_{rot} (\circ) \downarrow$ | $\bar{d}_{geo} \downarrow$ |
|---------------|------------------------------------|----------------------------|
| DINOv2-B [42] | 14.8 | 0.34 |
| Geo [64] | 10.4 | 0.35 |
| GECO (Ours) | 7.0 | 0.24 |

Table 8. **Quantitative Evaluation of Viewpoint Reconstruction and 2D-3D Matching.** We assess the quality of 2D-3D correspondences using the median rotation error \bar{e}_{rot} of the reconstructed view and mean geodesic distance \bar{d}_{geo} between matched and ground-truth keypoints. Our method outperforms DINOv2-B [42] and Geo [64] on both metrics, demonstrating superior performance in pose estimation and geometric reasoning. Best scores are shown in **bold**.

References

- [67] Alexander Kirillov, Eric Mintun, Nikhila Ravi, Hanzi Mao, Chad Rolland, Laura Gustafson, Trevor Xiao, Spencer Whitehead, Alexander C Berg, Wan-Yen Lo, Piotr Dollár, and Ross Girshick. Segment anything. *arXiv preprint arXiv:2304.02643*, 2023.
- [68] Gabriel L Oliveira, Abhinav Valada, Claas Bollen, Wolfram Burgard, and Thomas Brox. Deep learning for human part discovery in images. In *ICRA*, pages 1634–1641, 2016.
- [69] Silvia Zuffi, Angjoo Kanazawa, David W. Jacobs, and Michael J. Black. 3D Menagerie: Modeling the 3D Shape and Pose of Animals. In *CVPR*, pages 5524–5532, 2017.

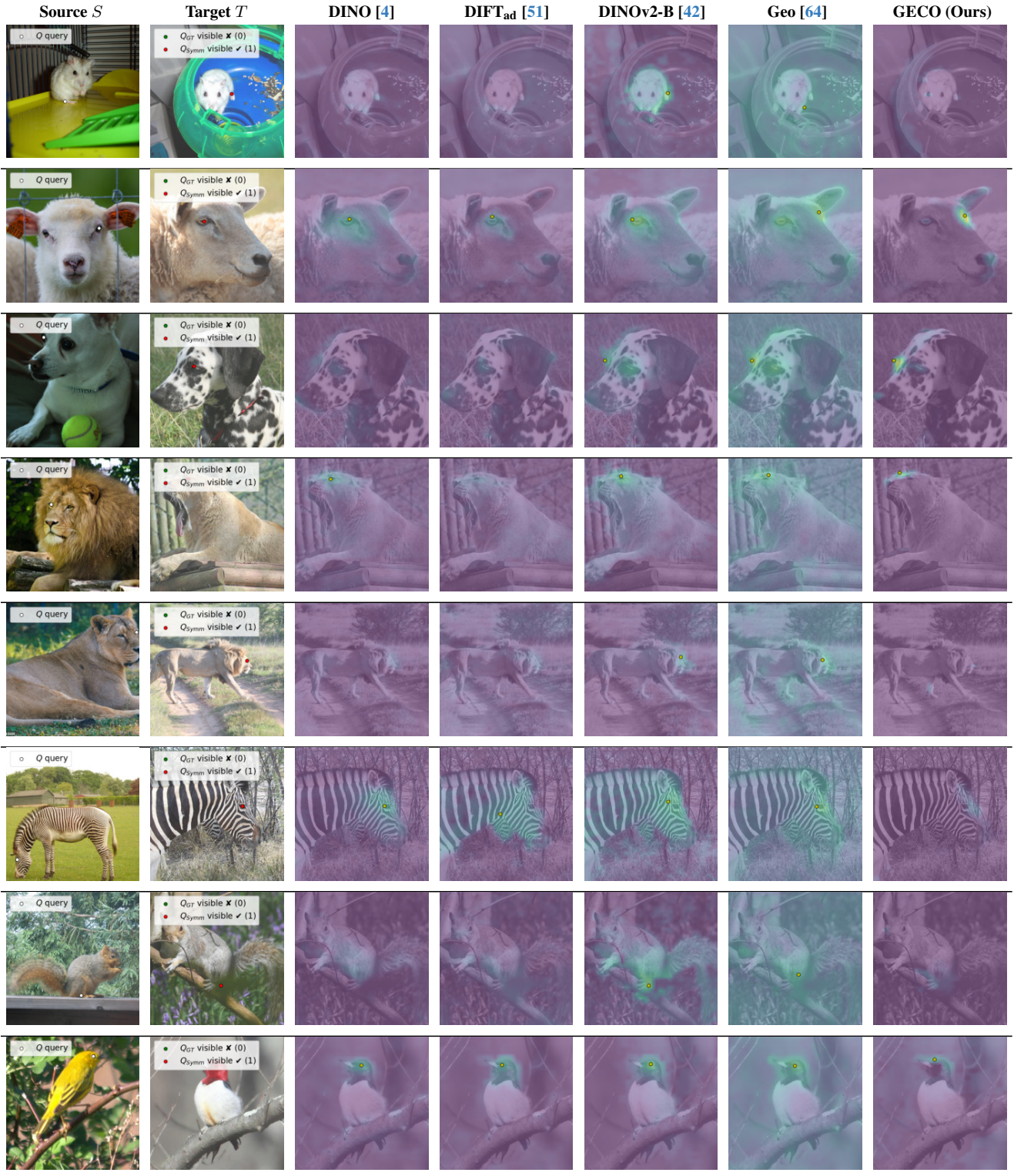


Figure 19. Qualitative results on the task of assignment to the bin (01-case) on APK [64] and CUB [55] (Last row).

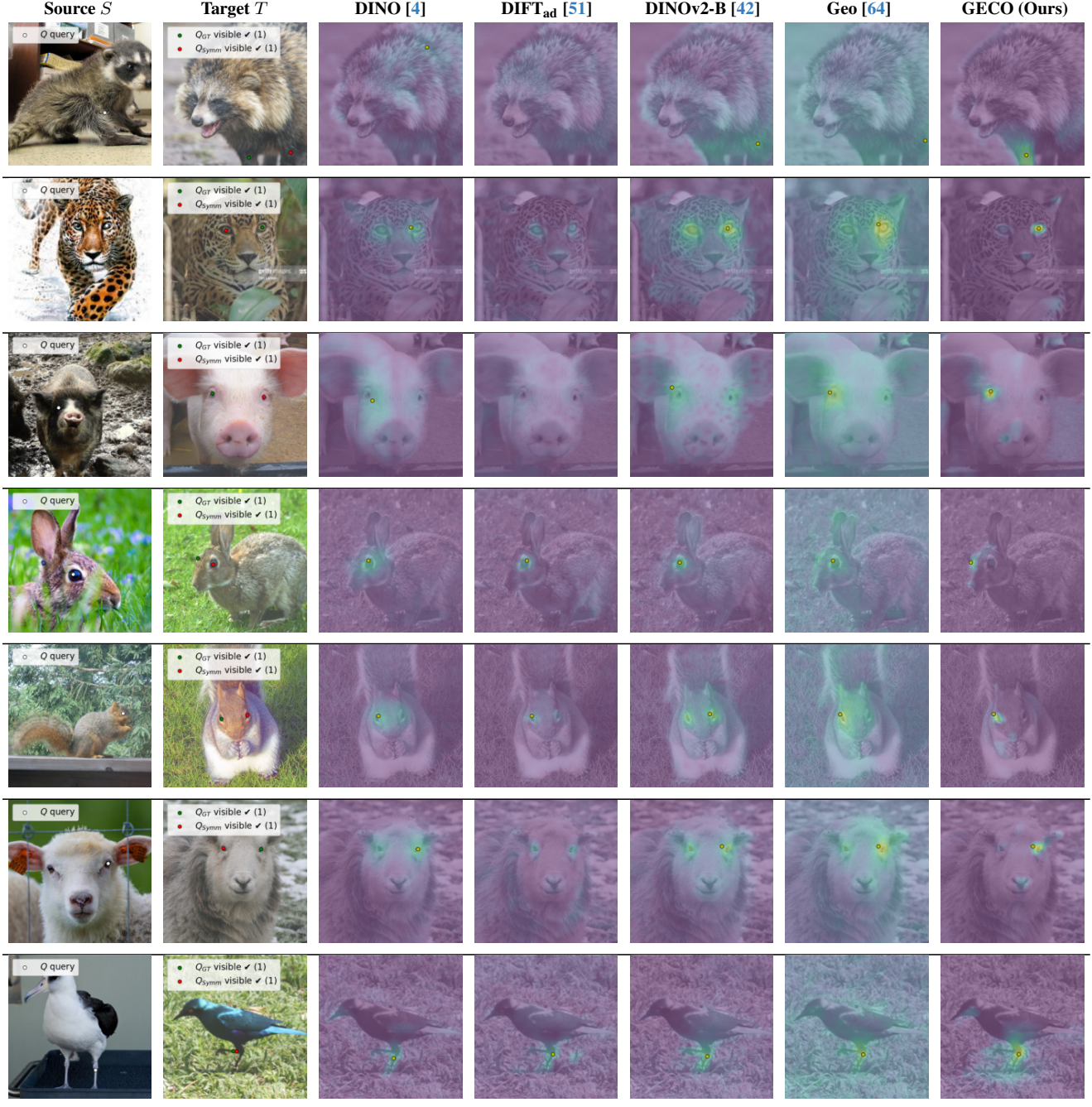


Figure 20. Qualitative results Qualitative results on the task of assignment to the correct correspondence (11-case) on APK [64], and CUB [55] (Last row). Note that the keypoint pair in the last row would be excluded in the unambiguous TP subdivision.

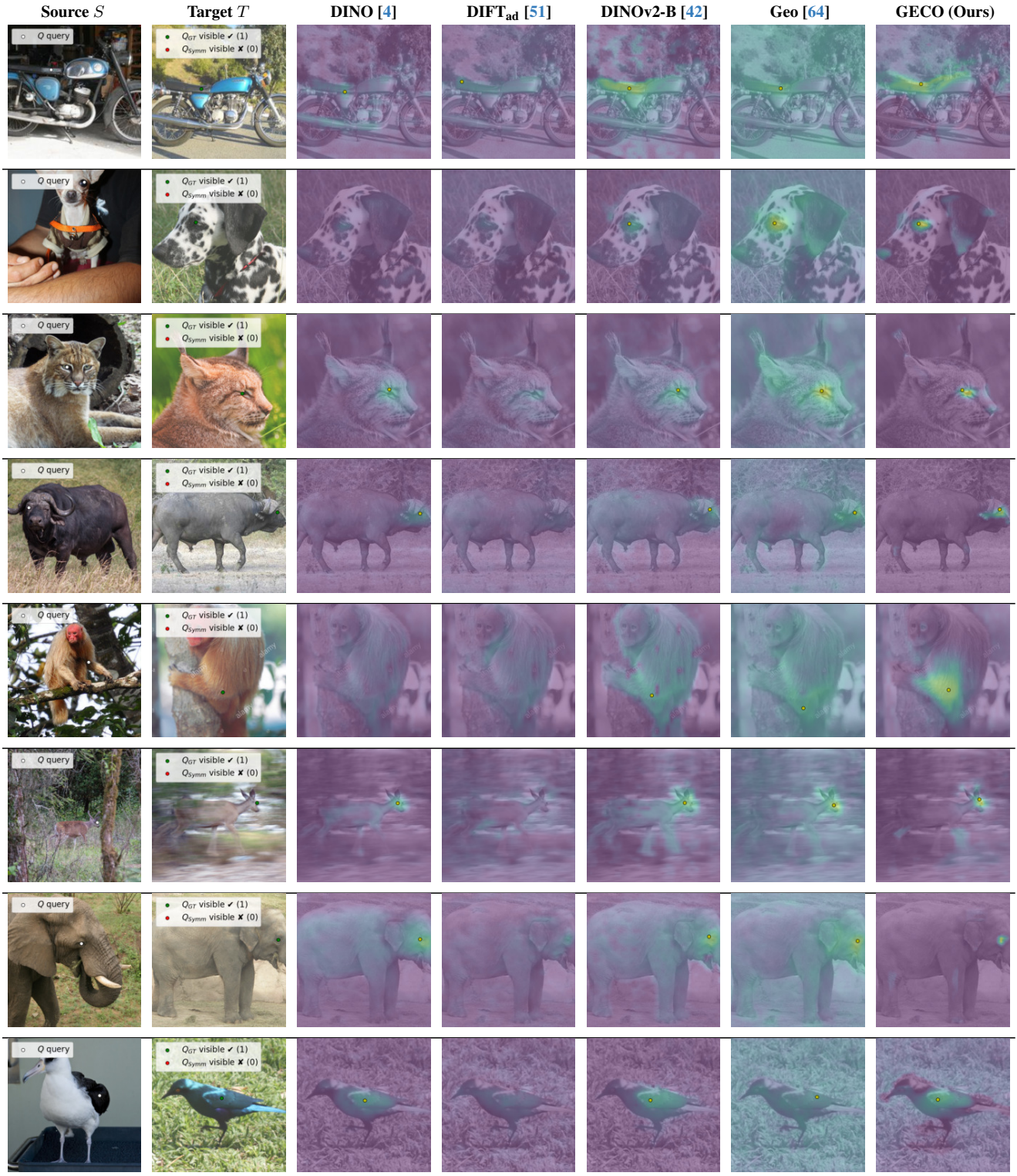


Figure 21. Qualitative results Qualitative results on the task of semantic correspondence estimation (10-case) on PFPascal [22] (First row), APK [64], and CUB [55] (Last row).